

# Dicke state preparation with applications in metrology

By

**Nabomita Roy Mukty**

A thesis submitted to Macquarie University  
for the degree of Master of Research  
Department of Department of Physics and Astronomy  
October 2019



**MACQUARIE**  
University  
SYDNEY · AUSTRALIA

Examiner's Copy



Except where acknowledged in the customary manner, the material presented in this thesis is, to the best of my knowledge, original and has not been submitted in whole or part for a degree in any university.

28.10.19

---

Nabomita Roy Mukty



# Acknowledgements

As I look back on my Masters degree, I cannot help but feel extremely fortunate to have been given the opportunity to work on such an exciting research project with the most incredible group of people. Firstly, I would like to express my deepest gratitude to the research team at Macquarie University that I am proud to be a part of. The biggest thanks goes to each of Gavin Brennen, Thomas Volz and Mattias Johnsson whose unwavering support in all aspects of my Masters degree is predominantly responsible for the successful completion of this thesis. Their brilliant academic guidance, kindness and an exceptionally positive attitude throughout this journey have made it an amazing experience. No words of praise are adequate to fully acknowledge their contribution in my growth as a researcher and my realization that the challenge of Physics is not only worthwhile but also enjoyable. Their brilliance, expertise and dedication as Physicists is truly inspiring and their zeal, contagious. I would also like to convey a special thanks to my MRes advisor Joanne Dawson, who has been a constant source of mental strength for me and the Head of our Department, Michael Steel for his continuing support at critical times. Finally, a huge thanks goes to my dear family and friends who love me unconditionally, have forever believed in me wholeheartedly and celebrate my passion for science just as much as I do. The single most important person without whom any accomplishment in my life would have been impossible is my sister, Bannya, who has consistently encouraged and inspired me to pursue my goals relentlessly. I am extremely lucky to have her as an invincible force of positivity through the laughter and the tears.



# Publication

- Mattias T. Johnsson, Nabomita Roy Mukty, Daniel Burgarth, Thomas Volz and Gavin K. Brennen, *Scalable preparation of Dicke states for quantum sensing*, 2019, (article in arXiv: 1908.01120v3 [quant-ph] 12 Aug 2019).





# Abstract

In this thesis, we focus on three distinct strategies to prepare Dicke states for quantum enhanced metrology. First, we consider an ensemble of spins with dipole-dipole interactions where we apply pulses to selectively climb up the Dicke ladder. In a second approach, we use geometric phase gates in a Grover method to obtain the Dicke states which does not require dipole-dipole interactions, selective addressing or special detunings and can accommodate large numbers of spins. The method's built-in protection against dephasing and the use of the prepared state for quantum metrology are discussed. For the third method, we consider spins coupled linearly to a bosonic mode and state preparation is investigated numerically through optimal control techniques with a combination of linear and non-linear controls. Our calculations largely focus on the preparation of the state in the middle of the Dicke ladder with half the spins excited and half de-excited, which is referred to as superradiant if emitting and superabsorptive when absorbing. Nonetheless, the methods can be applied to prepare any arbitrary Dicke state. This study will lead to the enrichment of knowledge regarding the theory of general Dicke state preparations and quantum control strategies while paving the way towards exciting applications in quantum precision metrology.



# Contents

<b>Acknowledgements</b>	<b>v</b>
<b>Publication</b>	<b>vii</b>
<b>Abstract</b>	<b>ix</b>
<b>Contents</b>	<b>xi</b>
<b>List of Figures</b>	<b>xiii</b>
<b>List of Tables</b>	<b>xv</b>
<b>1 Introduction</b>	<b>1</b>
1.1 Dicke state preparation . . . . .	2
1.2 Quantum precision metrology . . . . .	3
1.3 Superradiance . . . . .	4
1.4 Superabsorption . . . . .	5
1.5 Thesis structure . . . . .	7
<b>2 Dicke physics</b>	<b>9</b>
2.1 A single spin-1/2 system . . . . .	9
2.2 Collective dynamics of spin-1/2 systems . . . . .	10
2.2.1 Collective states of two spin-1/2 systems . . . . .	10
2.2.2 The Dicke states . . . . .	10
2.2.3 Superradiance . . . . .	12
2.3 Collective dynamics with dipole-dipole interactions . . . . .	14

<b>3</b>	<b>Method 1: Dicke state preparation using dipole-dipole interactions</b>	<b>17</b>
3.1	Dicke state preparation using a $\pi/2$ -pulse . . . . .	18
3.2	Dicke state preparation using successive $\pi$ -pulses . . . . .	20
3.3	Dipole-dipole interactions in spin ensembles . . . . .	20
3.3.1	Dipole-dipole interactions for a general arrangement of dipoles . . . . .	21
3.3.2	Dipole-dipole interactions for a ring of dipoles . . . . .	22
3.3.3	Dipole-dipole interactions for a line of dipoles . . . . .	24
3.4	Power broadening . . . . .	26
3.4.1	Calculating the maximum number of spins accounting for power broadening	27
<b>4</b>	<b>Method 2: Dicke state preparation using Grover method</b>	<b>29</b>
4.1	Spin-cavity dynamics for geometric phase gates in Grover method . . . . .	30
4.1.1	Single spin-cavity dynamics . . . . .	30
4.1.2	Multiple spin-cavity dynamics . . . . .	32
4.1.3	Geometric phase gates . . . . .	33
4.2	Details of our Grover method . . . . .	34
4.3	Decoherence effects . . . . .	37
4.3.1	Bosonic mode damping . . . . .	37
4.3.2	Dephasing and its suppression by dynamical decoupling . . . . .	37
4.4	Quantum metrology using Dicke states . . . . .	40
4.5	Implementation . . . . .	41
<b>5</b>	<b>Method 3: Dicke state preparation using optimal control techniques</b>	<b>43</b>
5.1	Spin-cavity dynamics for optimal control method . . . . .	43
5.2	Optimal control in QuTip . . . . .	45
5.3	Results . . . . .	46
<b>6</b>	<b>Conclusion</b>	<b>51</b>
<b>A</b>	<b>Appendix</b>	<b>55</b>
A.1	Alternative calculation to find total absorption rate for method 1. . . . .	55
	<b>References</b>	<b>59</b>

# List of Figures

2.1	The Dicke ladder for $N$ dipoles. The blue "rungs" are the degenerate Dicke states in absence of any interactions among dipoles. When dipole-dipole interactions are incorporated, they shift to red "rungs" which are non-degenerate. . . . .	12
2.2	Superradiance (red) of $N=10$ dipoles vs spontaneous emission (blue) of $N=10$ independent dipoles . . . . .	13
2.3	Schematic diagram of two dipoles interacting. . . . .	14
2.4	Energy splitting due to dipole-dipole interactions.. . . .	15
3.1	Probability distribution after state preparation with $J=40$ . Majority of the population is near the middle $ J, M = 0\rangle$ state. . . . .	19
3.2	Absorption rate after state preparation with $J=40$ . The rate is proportional to $J^2$ as expected of superabsorption. . . . .	19
3.3	Uniformly arranged ring of dipoles . . . . .	23
3.4	Change in differential energy shift for changing circumference of ring and number of dipoles, $N$ in the ring. . . . .	25
3.5	Uniformly arranged line of dipoles . . . . .	25
3.6	Change in differential energy shift for changing length and number of equidistant dipoles in a line, $N$ . . . . .	26
4.1	NV states as a qubit. . . . .	34
4.2	Closed loop formed by one geometric phase gate. . . . .	35
4.3	Geometric interpretation of application of Grover method to the initial state. . . . .	36
4.4	Spin echo effect that eliminates the effect of dephasing. . . . .	39

---

4.5	Phase uncertainty vs normalised mode decay for different values of $\Gamma_{\text{eff}}/\kappa = 0$ (light blue), $0.5 \times 10^{-3}$ (red), $1.0 \times 10^{-3}$ (yellow), $1.5 \times 10^{-3}$ (purple). This plot was produced by Dr Mattias Johnsson [1]. . . . .	41
5.1	Plot of control pulses after optimisation for $N=20$ spins. . . . .	47
5.2	Fidelity errors for number of spins from $N=2$ to 100, with a zoom inset from $N=2$ to 22. . . . .	48
5.3	Fidelity error comparison for different number of timeslots. . . . .	48
5.4	Fidelity error comparison for different number of trials. . . . .	49

# List of Tables

5.1	Input and output data of the optimisation algorithm for $N=20$ spins. . . . .	46
-----	---	----





*"You must have felt this too:  
the almost frightening simplic-  
ity and wholeness of the rela-  
tionships which nature suddenly  
spreads out before us and for  
which none of us was in the least  
prepared."*

- Werner Heisenberg

# 1

## Introduction

Dicke states are an important family of highly entangled quantum states[2–4] that are of extreme interest in theoretical and experimental quantum physics. More specifically, they have significant contributions in quantum metrology [5], quantum networking [6], quantum memories [7], quantum game theory [8] and quantum key distribution [9]. In this research project we have theoretically explored three methods to prepare Dicke states with an emphasis on its potential for tasks in quantum metrology. In Method 1 we explore how to use a  $\pi$ -pulse sequence on an ensemble of quantum spins to prepare Dicke states by climbing up the Dicke ladder step-by-step. In Methods 2 and 3 the spins are coupled to a common bosonic cavity mode and are described in the fully quantum mechanical picture. In particular, Method 2 uses dispersive coupling and a Grover algorithm while Method 3 uses linear coupling and quantum optimal control techniques for Dicke state preparation. These embody major concepts from quantum information, quantum computing and quantum control. We start this chapter by discussing some recent milestones in Dicke state preparation and describe its powerful capabilities for Heisenberg limited quantum metrology. We introduce the concept of superradiance which is an interesting and popular phenomenon of quantum enhanced emission exhibited by symmetrical states

in the middle of the Dicke ladder for a collection of identical emitters. Following this we discuss the less well-known reverse process of superradiance called superabsorption which, as the name suggests, refers to quantum enhanced rate of absorption by symmetrical states in the middle of the Dicke ladder. Quantum metrology, superradiance and superabsorption constitute three key applications of Dicke states, thereby primarily motivating the undertaking of this research project.

## 1.1 Dicke state preparation

Dicke states are entangled multi-spin quantum states which are describable as permutationally symmetric states in the maximum angular momentum space. The Dicke state  $|J, M\rangle$  is an entangled state of  $M + J$  excitations shared among  $N = 2J$  spins. The physics of Dicke states is discussed in details in Chapter 2. Dicke states have been experimentally created in various settings such as atoms [10–12], ions [13–15], photons [6, 16] and superconducting spins [17] but the effective preparation of arbitrary Dicke states with desirable circuit depth and scalability has only recently started to receive attention. The current best algorithm for the deterministic preparation of arbitrary Dicke states has a scaling of order  $O((\frac{N}{2} + M)N)$  gates and the circuit depth, i.e the measure of run time is  $O(N)$  [18], where  $N$  is the number of input qubits or spins in the system. This was even applicable to linear nearest neighbour arrangements which allows connection of each qubit to only its nearest neighbours instead of the more usual all-to-all connectivity. However, this method needs a set of universal quantum gates and individual qubit addressing. In a 2017 study by Wu et al [17], generation of Dicke states in the ultrastrong coupling regime was explored that did not require single spin addressability but there was a large detuning constraint to allow for selective resonant interaction. In their case, the inability to satisfy the detuning condition would cause a significant decrease in fidelity. In a study by Higgins et al [19], the details of which are discussed in section 1.4, dipole-dipole interactions were taken advantage of to break the Dicke degeneracy and create a ring structure of spins which allowed for unique transitions along the Dicke ladder to prepare Dicke states. However, interaction among the spins implies that states can mix with smaller  $J$ -spaces outside the Dicke space. There are also power broadening effects that may hamper scalability of this system for larger ensembles of spins. Compared to these methods, our Grover method as detailed in Chapter 4 will enable the preparation of the Dicke states without requiring selective addressing, dipole-dipole interactions, detuning constraints, irrespective of architecture of the physical system, with desirable scalability and circuit depth  $O(N^{\frac{5}{4}})$ . We can prepare any Dicke state with this method and it can be amended to suit a range of different physical

systems.

## 1.2 Quantum precision metrology

Measurement is the driving force behind all scientific advancements which has inspired the active research in high precision metrology. Quantum metrology is the science of using quantum theory and technologies to develop measurement tools which yield higher precision than possible in classical frameworks [20–22]. It is of vital importance for progress in high-precision research such as detection of gravitational waves and lowering frequency uncertainty in atomic clocks. Two important quantum phenomena that are useful for metrological applications are squeezing and entanglement. In this thesis, we focus on exploiting the latter in the form of Dicke states. Owing to their highly entangled nature, Dicke states are promising candidates to facilitate metrology beyond the shot noise limit of scaling  $1/\sqrt{N}$  which is the standard limit of precision for independent, unentangled probes and aim towards the lowest fundamental quantum bound called the Heisenberg limited precision of scaling  $1/N$ , where  $N$  is the number of probes or atoms [23]. The Heisenberg limit is possible for ideal, noise-free systems. However, all quantum systems in reality experience noise or decoherence. Thus, reducing decoherence is a difficult problem of intense interest in quantum metrology [24]. Recently there has been efforts to advance quantum metrology via quantum error corrections [25, 26]. Quantum error correction is a technique to protect against noise in quantum processors and channels, widely investigated in quantum computing and information science [27]. An example of such an endeavour include using error correction to prolong coherence times and thereby increasing quantum sensing ability by Arrad et al [28]. An interesting approach to subdue noise by preservation of Quantum Fisher information instead of protecting the quantum states themselves was devised by Lu et al [29]. In a paper by Zhou et al [30], they determine conditions to obtain the Heisenberg limit on noise characterised by a Markovian master equation, assuming noiseless ancillas, quantum gates and perfect measurements without obscuring the signal to be sensed. However, the control requirements for these schemes are complicated. There has also been interesting work in phase protected quantum metrology whereby symmetry-protection against errors in Haldane phase is utilized to devise a robust protocol to measure direction and strength of an electric field. But this requires engineering of interactions in physical systems such as Rydberg dressed atoms [31]. In comparison to these, our scheme for quantum sensing involves Dicke states prepared by using geometric phase gates (GPGs) that requires simpler controls and no interactions among dipoles with built-in protection against dephasing. Moreover, it is scalable

with high fidelities for large numbers of spins.

### 1.3 Superradiance

In the study of Dicke states superradiance is a popular topic. In fact, Dicke states were first studied by R.H. Dicke while investigating superradiance from a cloud of atoms in 1954 [32]. Superradiance describes the collective spontaneous decay of multiple quantum emitters whose spacing is smaller than the wavelength of light which leads to a higher photon flux for short times compared to independent decays. This short time photon flux is proportional to  $N^2$ , where  $N$  is the number of emitters. The quadratic dependence of emission intensity on the number of emitters is the key property to characterise superradiant behaviour. This behaviour is demonstrated exclusively by states in the middle of the Dicke ladder as the emitters couple to a common electromagnetic field. It is critical to note that this is in contrast to independent emission where the emitters interact non-coherently with the electromagnetic field and the total photon flux scales proportionally to  $N$ . Superradiance has been the subject of widespread investigation in theory [33–38] as well as experiment [39–44] ever since the pioneering paper by Dicke [32]. The results of the first detailed experimental investigation of Dicke superradiance were published about 20 years after Dicke’s prediction. In 1973, Skribanowitz et al observed superradiant bursts from optically pumped HF gas at room temperature and low pressure for the first time [39]. In 1976, Gross et al reported near-infrared superradiance from optically pumped sodium vapour [45]. Moi et al demonstrated superradiance in a system of Rydberg atoms in 1983 [46]. Superradiance in gases have been observed under a wide range of conditions by many other groups. The first solid state superradiance was demonstrated by Schmid et al in  $O_2^-$  centres in KCL crystals at low temperatures in 1982 [47]. Leontovich et al showed superradiance in YAG:Nd and ruby at 100 K between 1984-1986 [48, 49]. In 1996, DeVoe et al observed the first two-ion superradiance which is the most elementary experimental realization of Dicke’s theory [42]. Observation of superradiance from more recent years include interesting systems such as quantum dots by Scheibner et al in 2007 [50], superconducting qubits in a cavity by Mlynek et al in 2014 [43] and Nitrogen-Vacancy centre embedded single nanodiamonds at room temperature by Bradac et al in 2017 [44]. This is the first experiment to demonstrate superradiance from crystals much smaller than the wavelength of light and at room temperature. Very recently in 2018, Angerer et al studied superradiance in a system composed of a three-dimensional lumped element resonator coupled to nitrogen–vacancy centres in diamonds [51]. Due to persisting interest in such studies physicists have discovered a multitude of interesting

applications of superradiance. Some examples include exciton delocalisation in biological systems [52], novel laser technologies [53], single photon generation [54], quantum memories and quantum communication [55, 56]. Superradiance also has notable effects in astrophysics such as superradiant emission around blackholes [57].

## 1.4 Superabsorption

As we saw in the previous section, superradiance has been a widely studied topic in physics, whereas its reverse process, superabsorption has not seen as much research progress so far despite having great potential for exciting real-life applications in physics and medical science [19]. Although the methods described in this thesis can be largely used to prepare any Dicke state, in many cases, our calculations focus on the preparation of the  $|J, 0\rangle$  state in the middle of the Dicke ladder because it is capable of superabsorptive rates, i.e absorption rates that scale proportionally to  $N^2$ . We are inspired to explore this particular state because it can be used to create a superabsorbing system capable of the aforementioned applications in the future. Due to the quadratic dependence of absorption on number of spins, a superabsorbing system will be extremely sensitive to low levels of light. This will make it ideal as sensors in weak light fields that classical absorbers cannot detect. It can be utilized in microwave or optical sensors, in advanced cameras in the future or scientific equipment [19]. Superabsorbing systems can also be used for light harvesting. Turning the light absorbed from weak light fields into useful energy through an extraction process that is irreversible will be very beneficial. It can be used especially for wireless power transfer of light into areas that are not accessible by wired power transfer, for example, remote sensors and biological implants inside the body [19].

Owing to the time reversal symmetry of quantum mechanics, the observation of superradiance in certain systems means it is possible to see superabsorption in them as well. But in natural systems superabsorption is not likely to occur due to the dominance of emission over absorption as we assume there are no photons in vacuum for the system to absorb [19]. For superabsorption to take place, the system has to be prepared in a state that is halfway down the Dicke ladder, which is a ladder of symmetrical states that assumes atomic indistinguishability [32]. Thus, the  $|J, M = 0\rangle$  state is our desired superabsorbing state. Henceforth, we will refer to the emitters (or absorbers) as simply spins which will denote emitters or absorbers depending on the context. A possible system to observe superabsorption is an ensemble of spins in the shape of a ring as investigated by Higgins et al [19] and envisioned even earlier by Gross and Haroche [33] which uses interatomic interactions to vary

transition energies along the Dicke ladder but still preserves Dicke physics due to the special ring structure. In the absence of interactions among the dipoles, the transition energies between adjacent levels of the Dicke ladder are all the same. This makes it difficult to access the middle state, that is the superabsorbing state, since probing the system with light of a matching frequency can cause any of the other states except the  $M=J$  or all excited state to absorb the incoming photons at rates which are not quadratic in  $N$ . This can cause transition between any two adjacent Dicke states, instead of targetting the pair of our choice. Thus, the first task is to break this degeneracy of transition energies so that the transition of the superabsorbing state to the state just above it is unique and can be selectively accessed. This allows us to consider those two states as an effective two-level system that is superabsorbing. This is done by including dipole-dipole interactions among the spins which shifts the transition energies and therefore the transition frequencies by an amount that is dependent on the value of  $M$  which is different for every level of the ladder as shown in Figure 2.1. The dipole-dipole interaction Hamiltonian can be expressed as:

$$\hat{H}_{dd} = \Omega_{n,m} \sum_{n \neq m}^N (\hat{\sigma}_+^m \hat{\sigma}_-^n + \hat{\sigma}_-^m \hat{\sigma}_+^n), \quad (1.1)$$

where  $\Omega_{n,m}$  refer to the dipole-dipole interaction strength between the  $n$ th and  $m$ th spins. The first term in the Hamiltonian describes the loss of exciton by  $m$ th spin which is accompanied by a gain in exciton of the  $n$ th spin mediated through virtual photons. This is called exciton "hopping". The second term in the Hamiltonian represents the reverse of that since the Hamiltonian is energy-conserving and unitary. The dipole-dipole interaction strength can be defined as [33]:

$$\Omega_{n,m} = \frac{d^2}{4\pi\epsilon_0 r_{nm}^3} \left[ 1 - \frac{3(\hat{\mathbf{e}}_a \cdot \mathbf{r}_{nm})^2}{r_{nm}^2} \right] \sim \frac{d^2}{4\pi\epsilon_0 r_{nm}^3}, \quad (1.2)$$

where the  $\hat{\mathbf{e}}_a$  is the polarisation unit vector which is taken in this case to be perpendicular to the direction of the spins (plane of the spins), leading to the approximated expression on the right and  $\mathbf{r}_{nm}$  is the distance from  $n$ th to the  $m$ th spin. For large rings, accounting for only interactions between adjacent atoms is reasonable as  $\Omega$  falls as the cube of the distance between any two spins. The frequency shift for a general "down transition" from  $|J, M\rangle$  to  $|J, M-1\rangle$  is expressed as follows [19]:

$$\omega_{M \rightarrow M-1} = \omega_0 - 4\Omega \frac{M - \frac{1}{2}}{N - 1}, \quad (1.3)$$

where  $\omega_0$  is the bare atomic dipole transition frequency,  $\Omega$  is the dipole-dipole interaction strength between any two adjacent spins. The Dicke states are still a good eigenbasis for the system because of the highly symmetrical ring structure. With the spins equidistant from their adjacent ones and

their plane perpendicular to the polarisation vector of transition, this ring ensures that each of the spins are in the same environment subject to the same kind and degree of interactions so that they retain indistinguishability. The  $|J, M\rangle$  states with  $J = N/2$  are eigenstates of the symmetric dipole-dipole perturbation which means the dipole-dipole Hamiltonian,  $\hat{H}_{dd}$  does not mix these  $|J, M\rangle$  states with levels of lower symmetry characterised by eigenvalues of total angular momentum smaller than  $J = N/2$  [33]. In practical settings, the superabsorbing ring will not be perfect. There will be losses from the effective two level system, that is emission from the  $|J, M = -1\rangle$  state to the environment. To compensate for this loss, a reinitialization technique can be employed in which a chirped laser pulse is used to re-excite the system at regular intervals matching the natural lifetime of the loss, or through the more advanced technique of quantum feedback control [19].

## 1.5 Thesis structure

We start by introducing the physics of Dicke states in Chapter 2. This will lay the foundation for understanding the mathematical formalisms used throughout the thesis. Chapter 2 discusses the collective dynamics of two spins, multiple spins and how the dynamics changes in the presence of dipole-dipole interactions, where we analyse how these interactions break the degeneracy in the Dicke ladder. This will lead us to Chapter 3 where we exploit the property of non-degeneracy to cause selective transition using a sequence of  $\pi$ -pulses along the Dicke ladder to prepare Dicke states, in particular the  $|J, 0\rangle$  Dicke state which can be utilized to create a superabsorbing system. We consider a ring of spins, similar to the physical scenario analysed by Higgins et al [19]. However, unlike their work, our goal is not to prepare a superabsorbing system via reservoir engineering but only the specific state in the middle of the Dicke ladder that is capable of superabsorbing rates. Our calculations account for two new aspects, the first being the interactions between not only nearest neighbours but all dipoles and the second being the dependence of differential energy shift on spacing between dipoles and number of dipoles. We also model an additional arrangement of dipoles on a line and investigate system parameters similar to the ring structure case. We will refer to this as Method 1. An important aspect of state preparation is the scalability of the system. Thus, a mathematical analysis is carried out to figure out the maximum number of spins this scheme can accommodate before power broadening hampers the transition frequency resolution of our system and, therefore, render selective transition ineffective. We then propose and discuss an exciting and novel method of preparing a Dicke state in Chapter 4. This is Method 2 which uses geometric phase gates in a Grover method to generate the

Dicke state and out of all the three methods, Method 2 has been the most rigorously investigated in this research project. The effects of bosonic mode damping and global dephasing on state preparation are also considered and our method's built-in solution to this in the form of dynamical decoupling is discussed. We carry out analysis on the capability of the prepared states for quantum metrological tasks and conclude by exploring different physical systems that can utilize our scheme. In Chapter 5, we propose another method to prepare Dicke states by applying optimal control strategies to an ensemble of spins coupled linearly to a common bosonic mode and induced quadratic spin interaction. This is Method 3. Simulations are carried out in QuTip to optimise for the control pulse sequences required for state preparation and relationships such as fidelity error scaling with number of spins are explored. Finally, Chapter 6 summarizes the findings of this project, makes concluding remarks and presents possible future directions for our research.



*"All my life through, the new  
sights of Nature made me rejoice  
like a child. "*

- Marie Curie

# 2

## Dicke physics

This chapter will focus on the physics of collective angular momentum states for an ensemble of quantum mechanical spins. We will discuss the dynamics along the Dicke ladder which can show interesting quantum collective phenomena such as superradiance and the effect of dipole-dipole interactions on the degeneracy of the Dicke ladder.

### 2.1 A single spin-1/2 system

In quantum physics, the simplest non-trivial model for a quantum emitter or absorber is the two-level system [58]. Two-level systems can be used to describe a wide variety of physical systems including quantum dots [59], colour defect centres such as nitrogen vacancy centres [60] or silicon vacancy centres [61], electron spins or nuclear spins in solid state systems [62] and so on. In this thesis, we consider each quantum emitter as a spin-1/2 system, where the spin down or ground state with the angular momentum z-projection as  $-1/2$  is denoted by  $|g\rangle$ , and the spin up or excited state with the angular momentum z-projection as  $+1/2$  is denoted by  $|e\rangle$ . The ground state is assigned the lower

energy state,  $E_1$  and the excited state the higher energy state,  $E_2$ . The Hamiltonian for a single two-level system in the absence of interaction is called the bare atomic Hamiltonian and is written as  $\hat{H}_0 = |g\rangle\langle g| E_1 + |e\rangle\langle e| E_2$ . A two-level system can be described mathematically by the Pauli spin matrices which are given as

$$\sigma_x = |g\rangle\langle e| + |e\rangle\langle g| = \begin{pmatrix} 0 & 1 \\ 1 & 0 \end{pmatrix}, \sigma_y = i|g\rangle\langle e| - i|e\rangle\langle g| = \begin{pmatrix} 0 & -i \\ i & 0 \end{pmatrix}, \sigma_z = |e\rangle\langle e| - |g\rangle\langle g| = \begin{pmatrix} 1 & 0 \\ 0 & -1 \end{pmatrix},$$

where we have used vectors  $\begin{pmatrix} 0 \\ 1 \end{pmatrix} = |g\rangle$  and  $\begin{pmatrix} 1 \\ 0 \end{pmatrix} = |e\rangle$ . Now, we can rewrite  $\hat{H}_0$  as  $\hat{H}_0 = \frac{1}{2}(E_2 + E_1)\mathbb{1} + \frac{1}{2}(E_2 - E_1)\sigma_z = \frac{1}{2}\hbar\omega_0\sigma_z$ , where we can choose the zero point energy at will so that the mean of the two energies is 0, i.e.  $\frac{E_2+E_1}{2} = 0$  and  $\omega_0 = \frac{E_2-E_1}{\hbar}$  is the dipole transition frequency.

## 2.2 Collective dynamics of spin-1/2 systems

### 2.2.1 Collective states of two spin-1/2 systems

For two spin-1/2 systems or dipoles, the Hilbert space,  $H_{\text{total}}$  of the composite system is given by the tensor product of the two individual Hilbert spaces,  $H_1$  and  $H_2$  of the dipoles, i.e.  $H_{\text{total}} = H_1 \otimes H_2$ . Then the four possible states of the composite system are  $|ee\rangle, |eg\rangle, |ge\rangle, |gg\rangle$ . However, these states do not span the eigenbasis of the composite Hamiltonian. Thus, we can define 3 symmetric states  $|1, 1\rangle = |ee\rangle, |1, 0\rangle = (|eg\rangle + |ge\rangle)/\sqrt{2}, |1, -1\rangle = |gg\rangle$  and an anti-symmetric state  $|0, 0\rangle = (|eg\rangle - |ge\rangle)/\sqrt{2}$ . A convenient way to represent the states of a composite system consisting of multiple spins is the coupled or collective spin basis, where the states assume the form  $|J, M\rangle$  with  $J$  being the total angular momentum of the spins and  $M$  the  $z$ -projection of the total angular momentum, ranging from  $-J$  to  $J$  in integer steps.

### 2.2.2 The Dicke states

For a system with multiple dipoles, the coupled spin basis has an obvious advantage in describing the collective dynamics of the system as  $N$ , the number of dipoles become large. The Dicke states are a class of highly entangled collective states with the highest total angular momentum,  $J = N/2$ , for an ensemble of  $N$  spins that assume indistinguishability [32]. The states together form the Dicke ladder with  $N + 1$  rungs, as shown in Figure 2.1, where the highest rung corresponds to the highest energy state  $|J, J = N/2\rangle$  and the lowest rung to the lowest energy state  $|J, -J = -N/2\rangle$ . The rungs

are equidistant because this simple model assumes no dipole-dipole interactions between the emitters and therefore the transition energies between adjacent collective states or rungs along the ladder are the same. The general Dicke state,  $|J, M\rangle$  can be expressed as [33]:

$$|J, M\rangle = \frac{1}{\sqrt{\binom{2J}{J+M}}} \sum_{\pi} \underbrace{\left| \pi(g, \dots, g, e, \dots, e) \right\rangle}_{(J-M)} = \sqrt{\frac{(J+M)!(J-M)!}{(2J)!}} \sum_{\pi} \underbrace{\left| \pi(g, \dots, g, e, \dots, e) \right\rangle}_{(J-M)} \underbrace{\phantom{\left| \pi(g, \dots, g, e, \dots, e) \right\rangle}}_{(J+M)}, \quad (2.1)$$

where  $\sum_{\pi}$  represents the sum of all possible permutations and  $\binom{2J}{J+M}$  is the binomial coefficient associated with choosing  $(J+M)$  dipoles to be excited from a total of  $2J$  dipoles in the system.

To describe the dynamics of this system, henceforth we will use the collective angular momentum operators

$$\hat{J}^{\pm} = \sum_{i=1}^N \hat{\sigma}_i^{\pm}, \quad \hat{J}^z = \sum_{i=1}^N \hat{\sigma}_i^z, \quad \hat{J}^x = \frac{\hat{J}^+ + \hat{J}^-}{2}, \quad \hat{J}^y = \frac{\hat{J}^+ - \hat{J}^-}{2i} \quad (2.2)$$

where  $\hat{\sigma}_i^+ = |e\rangle \langle g|_i$ ,  $\hat{\sigma}_i^- = |g\rangle \langle e|_i$  and  $\hat{\sigma}_i^z$  are the individual spin-1/2 operators for the  $i$ th dipole. They satisfy the usual angular momentum commutation relations

$$[\hat{J}^+, \hat{J}^-] = 2\hat{J}^z, \quad [\hat{J}^z, \hat{J}^{\pm}] = \pm \hat{J}^{\pm}, \quad [\hat{J}^x, \hat{J}^y] = i\hat{J}^z, \quad [\hat{J}^y, \hat{J}^z] = i\hat{J}^x, \quad [\hat{J}^z, \hat{J}^x] = i\hat{J}^y \quad (2.3)$$

The collective operators act on the Dicke states as

$$\hat{J}_{\pm} |J, M\rangle = \sqrt{(J \pm M + 1)(J \mp M)} |J, M \pm 1\rangle \quad (2.4)$$

$$\hat{J}^z |J, M\rangle = M |J, M\rangle \quad (2.5)$$

The Hamiltonian of  $N$  identical spins in the absence of any light is expressed as  $\hat{H}_0 = \omega_0 \sum_{n=1}^N \hat{\sigma}_+^n \hat{\sigma}_-^n$ , where  $\omega_0$  is the bare atomic transition frequency, the Pauli operators are defined as  $\sigma_+^n = |e\rangle_n \langle g|$  and  $\sigma_-^n = |g\rangle_n \langle e|$  with  $|e\rangle_n$  and  $|g\rangle_n$  referring to the excited and ground states of the  $n$ th atom. In the presence of light, the light-system interaction Hamiltonian,  $\hat{H}_I$  is expressed in terms of the collective operators as  $\hat{H}_I = -\hat{E}d(\hat{J}_+ + \hat{J}_-)$ , where  $\hat{E}$  is the light field operator and  $d$  is the electric dipole matrix element of the atomic dipole transition. This interaction Hamiltonian,  $\hat{H}_I$  describes the evolution of the system as a so-called cascade down the Dicke ladder. We can then express the rate of this transition between adjacent states in the ladder as

$$\Gamma_{M \rightarrow M \pm 1} = \gamma_0 \langle J, M | \hat{J}^+ \hat{J}^- | J, M \rangle = \gamma_0 (J \pm M + 1)(J \mp M) = \gamma_0 \left(\frac{N}{2} \pm M + 1\right) \left(\frac{N}{2} \mp M\right), \quad (2.6)$$

where  $\gamma_0$  is the free atom decay rate defined as  $\gamma_0 = 8\pi^2 d^2 / 3\epsilon_0 \hbar \lambda^3$ , with  $\lambda$  as the wavelength of light.

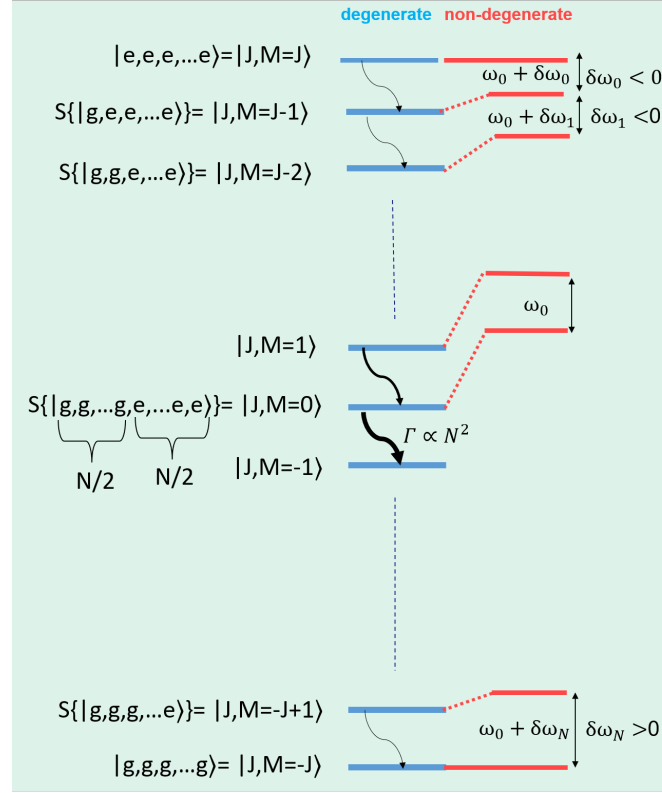


Figure 2.1: The Dicke ladder for  $N$  dipoles. The blue "rungs" are the degenerate Dicke states in absence of any interactions among dipoles. When dipole-dipole interactions are incorporated, they shift to red "rungs" which are non-degenerate.

### 2.2.3 Superradiance

Superradiance is a well-studied property of collective, coherent emission by states in the middle of the Dicke ladder. For an ensemble of identical emitters in a small volume without any decohering factors, the following conditions underlie the phenomenon of superradiance:

1. The emitters are spectrally indistinguishable.
2. The emitters are spatially indistinguishable.
3. The wavelength of light is greater than the distance between any two emitters. In fact, this final condition ensures that all the emitters are indistinguishable, so that light interacts with them collectively, resulting in a cooperative emission.

As the system cascades down the Dicke ladder, the rate of emission increases to a maximum  $\Gamma_{max} = \Gamma_{0 \rightarrow -1} \propto N^2$  which is obtained by putting  $M=0$  in the transition rate equation 2.6. This is superradiant emission, which is characterised by the rate scaling as  $N^2$ . This means if a system is initially in the fully excited state  $|J, M = J\rangle$ , the system has to cascade down to the  $|J, M = 0\rangle$  state at the middle

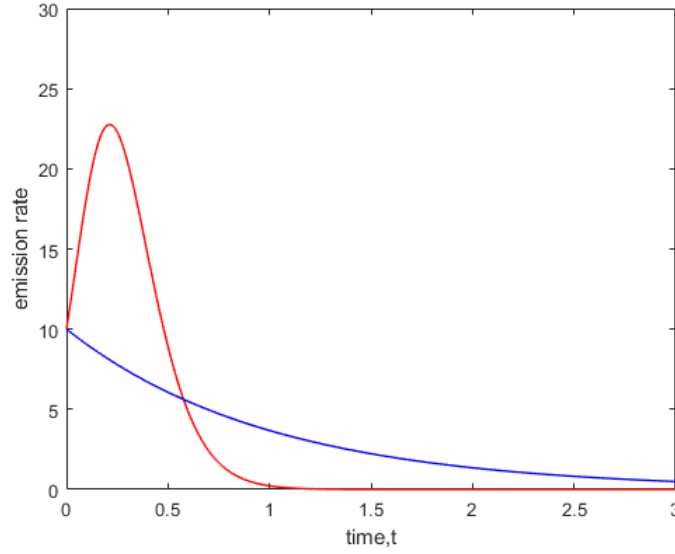


Figure 2.2: Superradiance (red) of  $N=10$  dipoles vs spontaneous emission (blue) of  $N=10$  independent dipoles

of the Dicke ladder to exhibit superradiance. At the middle there are a greater number of states in superposition that constitute the symmetrical state. This implies a greater number of possible decay paths that interfere constructively to give rise to an enhanced rate of emission. The collective emission of the system of dipoles can be described by the following master equation, as derived many times in peer-reviewed literature [[63],[35],[64]], involving the density matrix of the whole system,  $\rho$  and the collective operators,  $J^+$ ,  $J^-$ .

$$\frac{d\rho}{dt} = -\gamma_0(J^+ J^- \rho + \rho J^+ J^- - 2J^- \rho J^+) \quad (2.7)$$

This can be projected onto the Dicke states to give a differential equation in terms of the probability,  $P_M$  of finding the system in the  $|J, M\rangle$  state

$$\frac{dP_M}{dt} = -\gamma_0(J+M)(J-M+1)P_M + \gamma_0(J+M+1)(J-M)P_{M+1} \quad (2.8)$$

This equation can be solved in Matlab to produce a plot of the emission rate with respect to time from the system of spins, as shown in Figure 2.2. The emission rate increases with time as the collective system cascades down the Dicke ladder, reaching its maximum near the middle of the ladder and then decreasing.

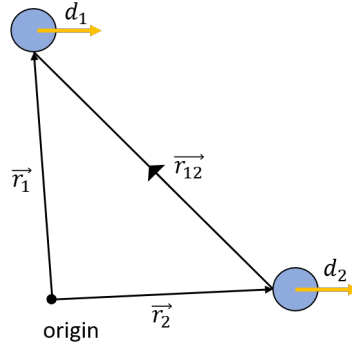


Figure 2.3: Schematic diagram of two dipoles interacting.

## 2.3 Collective dynamics with dipole-dipole interactions

An important consideration in the study of Dicke states is the interaction between dipoles. When this is taken into account, the Dicke ladder no longer remains degenerate and the collective states experience energy shifts as shown by the red ladder "rungs" in Figure 2.1. We will now discuss what this type of interaction looks like for two dipoles and how exactly the shifting of energy occurs.

The dipole-dipole interaction in the quantum scenario derives from that of the classical scenario. We start by picturing an interaction between dipoles as shown in Figure 2.3. When there is a single dipole, the potential energy is given by the Coulomb potential due to the inherent positive and negative charge distribution of the dipole but when there are multiple dipoles, we need to include the Coulomb potential of interaction between the two dipoles as well. Assuming the distance between the dipoles is much greater than the distances between poles inside each dipole, we get a total dipole-dipole interaction potential,  $V_{dd}$  given as [65]

$$V_{dd}(\vec{r}) = \frac{\vec{d}_1 \cdot \vec{d}_2 - 3(\vec{d}_1 \cdot \hat{n})(\vec{d}_2 \cdot \hat{n})}{r_{12}^3}, \quad (2.9)$$

where  $\vec{d}_1$ ,  $\vec{d}_2$  are dipole moments of dipole 1 and dipole 2 respectively,  $r_{12}$  is the distance between the dipoles and  $\hat{n}$  is the unit vector in the direction of  $r_{12}$ . We will assume the dipoles are parallel to each other which implies our equation 2.9 simplifies to  $V_{dd}(\vec{r}) = \frac{\vec{d}_1 \cdot \vec{d}_2}{r_{12}^3}$ . In the quantum mechanical picture, we can write the dipole moments as  $\vec{d}_1 = d(|e\rangle_1 \langle g| + |g\rangle_1 \langle e|)$  and  $\vec{d}_2 = d(|e\rangle_2 \langle g| + |g\rangle_2 \langle e|)$ , where  $d$  is the dipole moment strength. Using these expressions, we get  $V_{dd} = \frac{d^2}{r_{12}^3}(|e\rangle_1 \langle g| \otimes |g\rangle_2 \langle e| + |g\rangle_1 \langle e| \otimes |e\rangle_2 \langle g|)$ . Now, we can write the total Hamiltonian of the system as the sum of the bare atomic Hamiltonian,  $H_0 = \omega_0(|e\rangle_1 \langle e| + |e\rangle_2 \langle e|)$  and the dipole-dipole interaction potential  $V_{dd}$ .

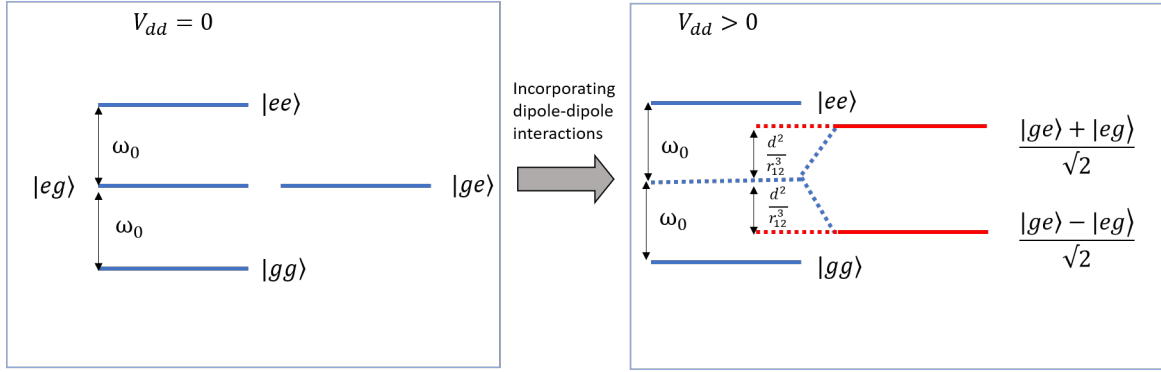


Figure 2.4: Energy splitting due to dipole-dipole interactions..

$$H_{\text{tot}} = \omega_0(|e\rangle_1 \langle e| + |e\rangle_2 \langle e|) + \frac{d^2}{r_{12}^3}(|e\rangle_1 \langle g| \otimes |g\rangle_2 \langle e| + |g\rangle_1 \langle e| \otimes |e\rangle_2 \langle g|) \quad (2.10)$$

In the absence of dipole-dipole interaction, i.e.  $V_{dd} = 0$ , the eigenstates of the system Hamiltonian were  $|gg\rangle, |ge\rangle, |eg\rangle, |ee\rangle$ . Of these the middle two eigenstates  $|ge\rangle, |eg\rangle$  had the same energy,  $\omega_0$  and hence were degenerate. However, as dipole-dipole interactions are taken into account, the new eigenstates are  $|gg\rangle, \frac{|ge\rangle + |eg\rangle}{\sqrt{2}}, \frac{|ge\rangle - |eg\rangle}{\sqrt{2}}, |ee\rangle$  with eigenvalues  $0, \omega_0 + \frac{d^2}{r_{12}^3}, \omega_0 - \frac{d^2}{r_{12}^3}, 2\omega_0$  respectively. The middle two eigenstates have experienced an upward and downward shift from the previous common energy value,  $\omega_0$  and are no longer degenerate. The breaking of the degeneracy is depicted in Figure 2.4. Similar to this case of two dipoles, for multiple dipoles, such interactions cause shifts in energies of all the collective Dicke states and give each pair of adjacent Dicke states a unique transition energy as shown in Figure 2.1.





*"If you are receptive and humble,  
mathematics will lead you by the  
hand."*

- Paul Dirac

# 3

## Method 1: Dicke state preparation using dipole-dipole interactions

In this chapter we will first explore a simple way to prepare the  $|J, 0\rangle$  Dicke state using a  $\pi/2$ -pulse. Secondly, we will discuss how we can use a sequence of  $\pi$ -pulses to climb up the Dicke ladder to prepare not only  $|J, 0\rangle$  but any Dicke state. This would require breaking the Dicke degeneracy by incorporating dipole-dipole interactions as introduced in Chapter 2. We will analyse different arrangements and numbers of dipoles to see how the dipole interactions vary and affect the energy shift of the Dicke states. Thus, for this  $\pi$ -pulse preparation method, we largely focus on the important requirement of accounting for dipole-dipole interactions. Finally, the effects of power broadening in this step-by-step state preparation are discussed.

### 3.1 Dicke state preparation using a $\pi/2$ -pulse

A very simple approach towards the preparation of the  $|J, 0\rangle$  state is to excite the collective ground state  $|J, -J\rangle$  by using a laser drive in the form of a  $\frac{\pi}{2}$ -pulse. A  $\pi$ -pulse has pulse area  $\Omega t = \pi$  and a  $\frac{\pi}{2}$ -pulse has pulse area  $\Omega t = \frac{\pi}{2}$ ,  $\Omega$  being the Rabi frequency and  $t$  the duration of the pulse. For a single two-level dipole, applying a  $\pi$ -pulse flips it from ground to excited state and a  $\frac{\pi}{2}$ -pulse puts it in a superposition of the ground and excited state. Our system consists of  $N$  two-level dipoles in a symmetric space which corresponds to a Dicke ladder of  $N + 1$  collective states. Analogous to the single two-level atom case, if a  $\pi$ -pulse is applied to this  $N + 1$ -level system, it will undergo total inversion, i.e. it can be driven from  $|J, -J\rangle$ , where all dipoles are de-excited, to  $|J, J\rangle$ , where all dipoles are excited. However, driving it with a  $\frac{\pi}{2}$ -pulse will non-uniformly spread the population across all  $|J, M\rangle$  states instead of placing it in any one particular state, with majority of the population being in the  $|J, 0\rangle$  state, where half the dipoles are excited and half are de-excited. This probability distribution is shown in Figure 3.1.

The light-matter interaction Hamiltonian of the driving laser and the system is given by  $H_{\text{int}} = J^y$  and the resulting state is expressed as  $|\Psi\rangle = e^{i\frac{\pi}{2}J^y}$ . To confirm that this is indeed a superabsorbing state, we will show that the rate of absorption of light in this state is proportional to  $N^2$ . The absorption rate,  $\Gamma_\Psi$  can be calculated as

$$\begin{aligned}
 \Gamma_\Psi &= \sum_{M=-J}^J \left( P(M) \times \langle J, M | J^- J^+ | J, M \rangle \right) \\
 &= \sum_{M=-J}^J \left( \left| \langle J, M | e^{i\frac{\pi}{2}J^y} | J, -J \rangle \right|^2 \times \left( (J - M)(J + M + 1) \right) \right) \\
 &= \sum_{M=-J}^J \left( \left( \sum_{k=0}^{2J} (-1)^{k-M-J} \frac{\sqrt{(J+M)!(J-M)!(2J)!}}{(M+J-k)!k!(2J-k)!(k-M-J)!} \right. \right. \\
 &\quad \left. \left. \cos\left(\frac{\pi}{4}\right)^{3J-2k+M} \sin\left(\frac{\pi}{4}\right)^{2k-M-J} \right|^2 \times \left( (J - M)(J + M + 1) \right) \right) \quad (3.1)
 \end{aligned}$$

where  $P(M)$  is the probability distribution of Dicke states after excitation from  $|J, -J\rangle$  and  $\langle J, M | J^- J^+ | J, M \rangle = (J - M)(J + M + 1)$  is the excitation rate between adjacent states of the Dicke ladder. The expression for  $P(M)$  is found by using a closed formula for rotation matrices called Wigner's formula [66]. A plot of  $P(M)$  in Figure 3.1 shows that the probability of being in  $M=0$  state is the highest after state preparation. The absorption rate in this prepared state,  $\Gamma_\Psi$  is plotted against  $J = \frac{N}{2}$  in Figure 3.2, which shows a quadratic increase of rate, as we would expect for a superabsorbing state. In both the plots, the number of dipoles is taken to be 80, ie,  $N = 80$  and  $J = \frac{80}{2} = 40$ . We can

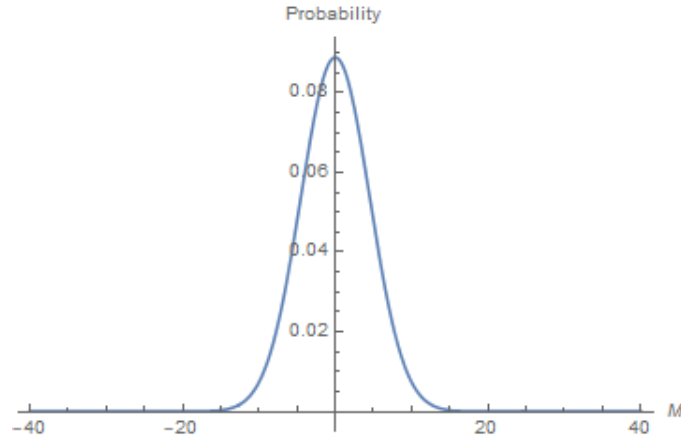


Figure 3.1: Probability distribution after state preparation with  $J=40$ . Majority of the population is near the middle  $|J, M = 0\rangle$  state.

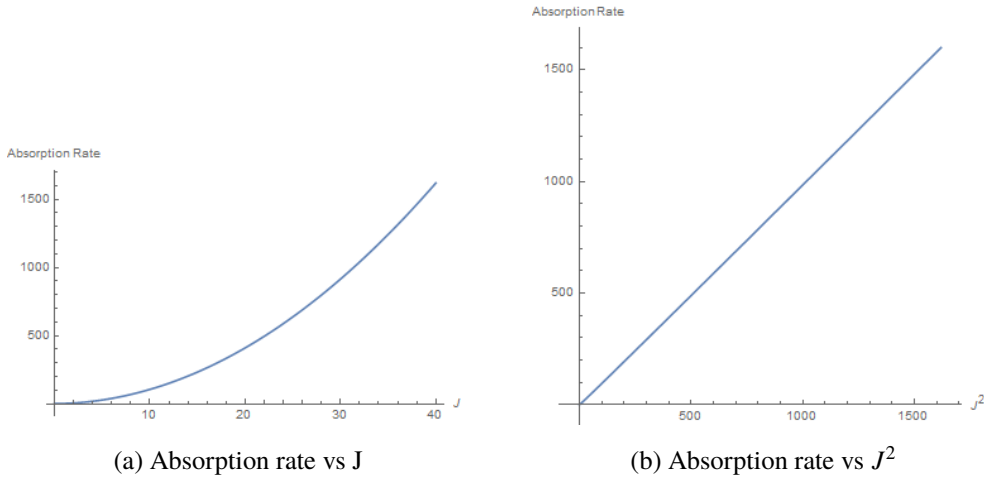


Figure 3.2: Absorption rate after state preparation with  $J=40$ . The rate is proportional to  $J^2$  as expected of superabsorption.

also work out an exact form for the absorption rate,  $\Gamma_\Psi$ , the details of which are presented in Appendix A.1. The exact form is

$$\Gamma_\Psi = \gamma(J^2 + \frac{J}{2}) \quad (3.2)$$

When we compare the absorption rate from this prepared state,  $|\Psi\rangle$  to the absorption rate from the ideal Dicke state,  $|J, 0\rangle$  we notice that they are very close. The rate from  $\pi/2$ -pulse prepared state,  $|\Psi\rangle$  is  $\Gamma_\Psi = \gamma(J^2 + \frac{J}{2})$  and the rate from the ideal Dicke state,  $|J, 0\rangle$  is  $\Gamma_{M=0} = \gamma(J^2 + J)$ . However, it is critical to note that even though the absorption rates are similar, as an absorption event takes place the transition from the prepared state to higher states will not be discrete because the prepared state has populations distributed across the different levels of the Dicke ladder. This is evident from the

probability values,  $P(M)$  after state preparation. For  $J = 40$ , i.e.  $N = 80$  spins, we can see in Figure 3.1 that the probability for the state being in  $M = 0$  level is merely 0.0889279. This can be taken as a measure of fidelity which determines how close the prepared state is to the ideal target quantum state [67]. Low fidelity means the detection of an absorption event by this state will be much harder as it will not show a sharp absorption spectrum. Thus, while a  $\pi/2$ -prepared state theoretically shows quantum-enhanced rates of absorption that scales quadratically with the number of spins, it cannot be used to detect weak light fields. The other two methods which we will discuss in Chapter 4 and Chapter 5 are much more sophisticated and will be aimed at preparing Dicke states with high fidelities.

### 3.2 Dicke state preparation using successive $\pi$ -pulses

As we saw in the previous section, using a single  $\pi/2$ -pulse to cause a transition from the ground Dicke state to the  $|J, 0\rangle$  Dicke state gives a low fidelity. A better approach would be to use a succession of  $\pi$ -pulses to climb the Dicke ladder in steps by causing transitions between two adjacent Dicke states with a  $\pi$ -pulse applied at every step. Furthermore, we can prepare not only  $|J, 0\rangle$  but any Dicke state with this approach. This means if our initial state is the ground Dicke state,  $|J, -J\rangle$  and the target state is any arbitrary state  $|J, M = K\rangle$  with  $K \in [-J + 1, J]$ , we want the following sequence of transitions.

$$|J, -J\rangle \xrightarrow{\pi\text{-pulse}} |J, -J + 1\rangle \xrightarrow{\pi\text{-pulse}} \dots\dots\dots |J, K - 1\rangle \xrightarrow{\pi\text{-pulse}} |J, K\rangle$$

However, to enable this it is essential to address any pair of adjacent Dicke states specifically. As we have already seen in Chapter 2 incorporating dipole-dipole interactions breaks the Dicke degeneracy which makes it possible to cause specific transitions between any two adjacent states of our choice. This is the motivation behind the next section of this chapter that discusses the result of accounting for dipole-dipole interactions in an ensemble of spins for different arrangements and the calculation of shifts in transition energies. It is important to note that this step-by-step preparation method is subject to power broadening effects which will make it difficult to resolve the unique transition frequencies. This will be addressed later in section 3.4.

### 3.3 Dipole-dipole interactions in spin ensembles

Here, we will analyse dipole-dipole interactions in circular and linear structures, accounting for interactions between not only nearest neighbours but all dipoles. We will find the shift in energy of the Dicke states that these interactions give rise to and discuss how the energy shift changes with dipole

spacing and number. This study on dipole interactions was inspired by the paper by Higgins et al [19]. However, compared to them, we explore the effects of these interactions on the Dicke ladder in more details, considering not only nearest neighbour interactions but interactions among all spins and linear structures in addition to ring structures. We also analyse how these effects vary with the number and spacing of the dipoles.

### 3.3.1 Dipole-dipole interactions for a general arrangement of dipoles

For a general arrangement of dipoles, the interaction Hamiltonian,  $V_{dd}$  is given by:

$$V_{dd} = \sum_{j \neq k} f(j, k) (\sigma_j^+ \sigma_k^- + \sigma_j^- \sigma_k^+), \quad (3.3)$$

where  $j$  and  $k$  are the sites of any two dipoles and  $f(j, k)$  is the strength of interaction energy between the  $j$ th and  $k$ th dipoles. The interaction Hamiltonian represents the total energy of the system of dipoles, which is a conserved quantity. The term  $(\sigma_j^+ \sigma_k^- + \sigma_j^- \sigma_k^+)$  describes the exchange of excitation among the dipoles such that if the  $j$ th dipole gains excitation, the  $k$ th dipole loses excitation and vice versa, so as to conserve the total number of excitations in the system. To find the shift in energies in the Dicke ladder due to the dipole-dipole interactions, we will require this interaction Hamiltonian. The shift will be given by the matrix elements of  $V_{dd}$  in the  $|J, M\rangle$  basis as follows:

$$\begin{aligned} \delta E_M &= \langle J, M | V_{dd} | J, M \rangle \\ &= \sum_{j \neq k} f(j, k) \langle J, M | (\sigma_j^+ \sigma_k^- + \sigma_j^- \sigma_k^+) | J, M \rangle \\ &= \sum_{j \neq k} f(j, k) \langle J, M | (\sigma_1^+ \sigma_2^-) | J, M \rangle \times 2 \\ &= \sum_{j \neq k} f(j, k) \left( \frac{J^2 - M^2}{2J(2J - 1)} \right) \times 2 \\ &= \sum_{j \neq k} f(j, k) \frac{(\frac{N}{2})^2 - M^2}{N(N - 1)} \times 2 \end{aligned} \quad (3.4)$$

To get the expression for  $\langle J, M | (\sigma_1^+ \sigma_2^-) | J, M \rangle$  in equation 3.4, we start with our general expression for  $|J, M\rangle = \frac{1}{\sqrt{\binom{2J}{J+M}}} \sum_{\pi} \underbrace{\pi(g, \dots, g)}_{(J-M)} \underbrace{\pi(e, \dots, e)}_{(J+M)}$ , which can be re-written by taking two dipoles out of the

symmetrization term,  $|\pi(g, \dots g, e, \dots e)\rangle$  and writing the possible permutations explicitly as:

$$\begin{aligned}
 |J, M\rangle = \frac{1}{\sqrt{\binom{2J}{J+M}}} & \left[ |e, e\rangle \sum_{\pi \in S_1} \underbrace{\left| \pi(g, \dots g, e, \dots e) \right\rangle}_{(J-M) \quad (J+M-2)} + |e, g\rangle \sum_{\pi \in S_2} \underbrace{\left| \pi(g, \dots g, e, \dots e) \right\rangle}_{(J-M-1) \quad (J+M-1)} \right. \\
 & \left. + |g, e\rangle \sum_{\pi \in S_3} \underbrace{\left| \pi(g, \dots g, e, \dots e) \right\rangle}_{(J-M-1) \quad (J+M-1)} + |g, g\rangle \sum_{\pi \in S_4} \underbrace{\left| \pi(g, \dots g, e, \dots e) \right\rangle}_{(J-M-2) \quad (J+M)} \right], \quad (3.5)
 \end{aligned}$$

Here  $S_1, S_2, S_3$  and  $S_4$  are simply the sets for permutation of the dipoles remaining inside the symmetrization operator. When  $\sigma_1^+ \sigma_2^-$  is applied to the above form of the general Dicke state, there's only one non-zero term:

$$\begin{aligned}
 \langle J, M | (\sigma_j^+ \sigma_k^- + \sigma_j^- \sigma_k^+) | J, M \rangle &= \frac{1}{\sqrt{\binom{2J}{J+M}}} |S_2| = \frac{1}{\binom{2J}{J+M}} \binom{2J-2}{J+M-1} \\
 &= \frac{(2J-2)!}{(J+M-1)!(2J-2-(J+M-1))!} \\
 &= \frac{(2J)!}{(J+M)!(2J-J-M)!} \\
 &= \frac{J^2 - M^2}{2J(2J-1)} \\
 &= \frac{(\frac{N}{2})^2 - M^2}{N(N-1)} \quad (3.6)
 \end{aligned}$$

where  $|S_2|$  is the binomial coefficient associated with choosing  $J + M - 1$  excitations from  $2J - 2$  dipoles for the state within symmetrization term in set  $S_2$  in equation 3.5. As we can see, the energy shift is dependent on the total number of dipoles in the system,  $N$  and the value of  $M$  which signifies the different rungs of the Dicke ladder. This implies every pair of rungs will have different energy shifts which will successfully break the Dicke degeneracy.

The next step is to determine how the energy shift,  $\delta_M$  varies for different arrangements such as a ring and a line of dipoles. It is interesting to note that for both the ring and line arrangements, the summation over the excitation exchange terms,  $(\sigma_j^+ \sigma_k^- + \sigma_j^- \sigma_k^+)$  gives the same result. However, summation over the interaction strength term,  $f(j, k)$  varies with the type of arrangement. Thus, in the next subsections, we will analyse the interaction strength term and the energy shift for a ring of uniformly arranged dipoles and a line of uniformly arranged dipoles.

### 3.3.2 Dipole-dipole interactions for a ring of dipoles

If the dipole-dipole interaction is present in a system where the dipoles are arranged in a symmetrical shape such as a ring, the dipoles still experience the same environment. The degeneracy of the Dicke

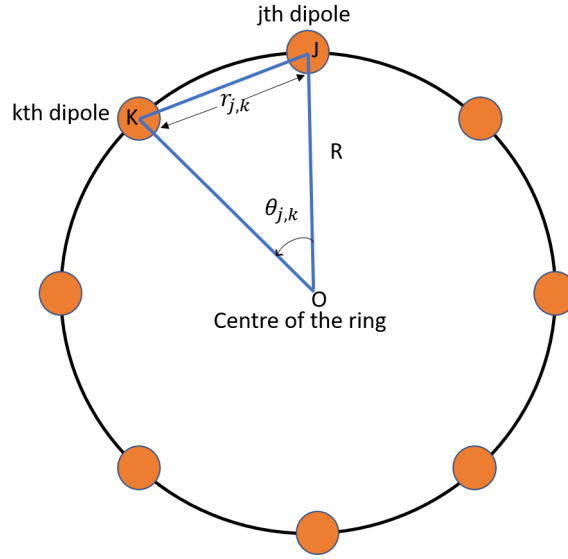


Figure 3.3: Uniformly arranged ring of dipoles

ladder is broken but the dipoles can still be described by the symmetric  $J$ -space, i.e they retain dipole permutation symmetry [33]. In general, the interaction strength between two dipoles at sites  $j$  and  $k$  is given by  $f(j, k) = \frac{d^2}{|r_j - r_k|^3} = \frac{d^2}{r_{j,k}^3}$ , where  $r_j - r_k$  is the distance between the  $j$ th and  $k$ th dipoles which is a positive number. So, the modulus is taken and it is re-written as  $r_{j,k}$ . For a ring structure, the dipoles can be envisioned to be point particles arranged uniformly as shown in Figure 3.3, where each dipole interacts with all the other dipoles. The angle,  $\theta_{j,k}$  between two dipoles can be expressed in terms of the number of dipoles,  $N$ . The distance,  $r_{j,k}$  between any two dipoles can be expressed in terms of the radius from the centre of the ring to a dipole,  $R$  and  $\theta_{j,k}$  by performing some basic trigonometry on the triangle  $\Delta OJK$  as  $r_{j,k} = 2R \sin\left(\frac{\theta_{j,k}}{2}\right) = 2R \sin\left(\frac{\pi|(k-j)|}{N}\right)$  with  $\theta_{j,k} = \frac{2\pi}{N}|(k-j)|$ . Now, the energy shift,  $\delta E_M$  can be obtained by substituting this  $r_{j,k}$  into equation 3.4 for a ring of dipoles as:

$$\begin{aligned}
 \delta E_M &= \sum_{j \neq k} \frac{d^2}{\left(2R \sin\left(\frac{\pi|(k-j)|}{N}\right)\right)^3} \frac{\left(\frac{N}{2}\right)^2 - M^2}{N(N-1)} \times 2 \times N \\
 &= \sum_{k=1}^N \frac{d^2}{\left(2R \sin\left(\frac{\pi|(k-1)|}{N}\right)\right)^3} \frac{\left(\frac{N}{2}\right)^2 - M^2}{N(N-1)} \times 2 \times N \\
 &= \sum_{k=1}^N \frac{d^2}{\left(\frac{C}{\pi} \sin\left(\frac{\pi|(k-1)|}{N}\right)\right)^3} \frac{\left(\frac{N}{2}\right)^2 - M^2}{N(N-1)} \times 2 \times N, \tag{3.7}
 \end{aligned}$$

where we have expressed the radius,  $R$  in terms of the circumference,  $C$  of the ring in the final line of the equation. We will now use  $\delta E_M$  to find the differential energy shift,  $\delta E_{M,M-1}$  i.e. the shift of

transition energies between two adjacent rungs of the Dicke ladder. This value will tell us the exact energy difference and therefore frequency difference between any two adjacent Dicke states, which then can be used to determine the frequency of our laser drive to generate the desired transition in the Dicke ladder.

$$\begin{aligned}
\delta E_{M,M-1} &= \delta E_M - \delta E_{M-1} \\
&= \langle J, M | V_{dd} | J, M \rangle - \langle J, M-1 | V_{dd} | J, M-1 \rangle \\
&= - \sum_{j \neq k} f(j, k) \frac{(2M-1)}{\left(\frac{N}{2}\right)(N-1)}
\end{aligned} \tag{3.8}$$

If we consider the transition from  $|J, -1\rangle$  to the superabsorbing state  $|J, 0\rangle$  for this ring of dipoles, the differential energy shift is:

$$\delta E_{0,-1} = \sum_{k=1}^N \frac{1}{\left(\frac{C}{\pi} \sin\left(\frac{\pi|(k-1)|}{N}\right)\right)^3} \frac{1}{\left(\frac{N}{2}\right)(N-1)} \times N, \tag{3.9}$$

where it should be noted that we have taken  $d = 1$  for simplicity. An interesting analysis is to check how the differential energy shift changes with the spacing between the dipoles and the number of dipoles. As we see in Figure 3.4a, the differential energy shift decreases rapidly with increasing circumference of the ring with the number of dipoles kept constant at  $N=30$ . Since the dipoles are uniformly arranged, increasing the circumference of the ring while keeping the number of dipoles unchanged implies that the dipoles are getting further apart, resulting in weaker interactions among the dipoles, thereby causing the differential energy shifts in the Dicke ladder to become smaller. Figure 3.4b shows that the differential energy shift increases at an increasing rate with the number of dipoles for a fixed circumference of ring at  $C = 5\pi$  units. As the number of dipoles increases while the circumference of the ring is kept unchanged, dipoles become closer to each other and each dipole interacts with more dipoles. This leads to the net interaction energy of the whole ensemble of dipoles to increase and cause greater differential energy shifts in the Dicke ladder.

### 3.3.3 Dipole-dipole interactions for a line of dipoles

For a uniform linear arrangement, the dipoles can be envisioned as shown in Figure 3.5 where each dipole interacts with all the other dipoles. The total length of the chain is  $L$  and the distance between  $j$ th dipole and  $k$ th dipole is  $r_{j,k}$ , which can be written in terms of  $L$  and total number of dipoles,  $N$  as  $r_{j,k} = |(k-j)| \frac{L}{(N-1)}$ . Now, the energy shift,  $\delta E_M$  can be obtained by substituting  $r_{j,k}$  into equation 3.4



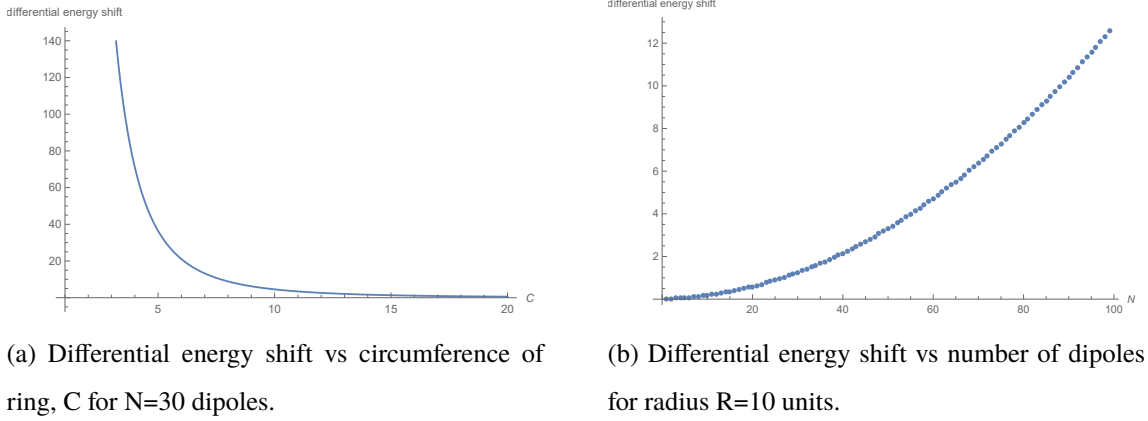


Figure 3.4: Change in differential energy shift for changing circumference of ring and number of dipoles, N in the ring.

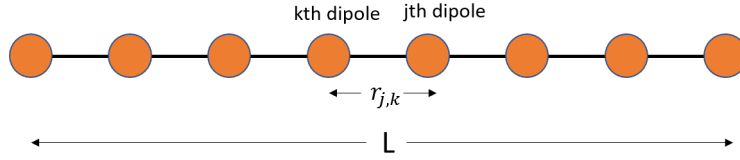


Figure 3.5: Uniformly arranged line of dipoles

for a line of dipoles as:

$$\delta E_M = \sum_{j \neq k} \frac{d^2}{\left( |(k-j)| \frac{L}{(N-1)} \right)^3} \frac{\left( \frac{N}{2} \right)^2 - M^2}{N(N-1)} \times 2 \times N \quad (3.10)$$

Similar to our ring case, we can now find the differential energy shift for transition from  $|J, -1\rangle$  to  $|J, 0\rangle$  for our line of dipoles:

$$\delta E_{0,-1} = \sum_{j \neq k} \frac{1}{\left( |(k-j)| \frac{L}{(N-1)} \right)^3} \frac{1}{\left( \frac{N}{2} \right)(N-1)}, \quad (3.11)$$

where we have once again taken  $d = 1$  for simplicity. We can plot this differential energy shift against length of the line while keeping the number of dipoles constant as shown in Figure 3.6a. We see a rapid decrease of the differential energy shift as the length of the line increases, quite similar to that of the ring structure. Increasing the length of the whole line increases the distance between the dipoles while the number of dipoles are kept fixed. The further apart the dipoles are the less strongly they

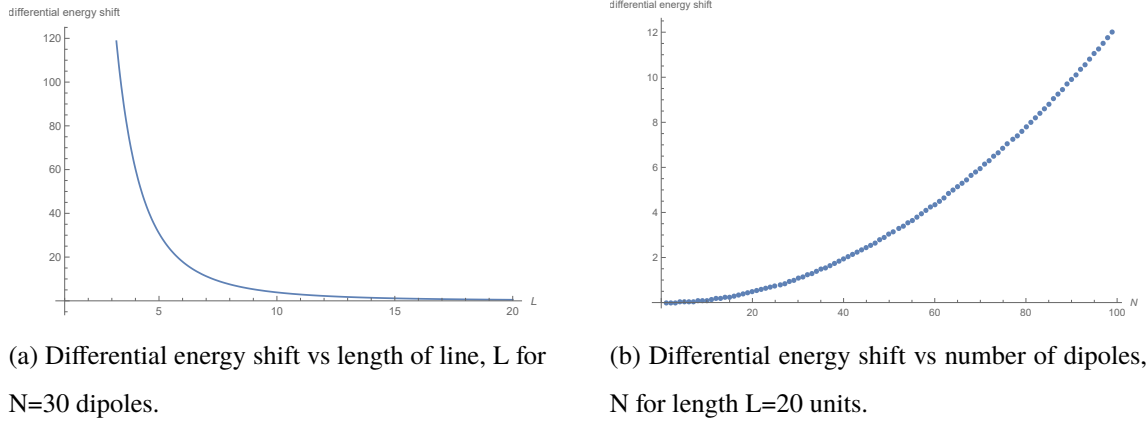


Figure 3.6: Change in differential energy shift for changing length and number of equidistant dipoles in a line,  $N$ .

interact and the net total interaction energy falls fast, giving smaller differential energy shifts. Figure 3.6b shows an increase in differential energy shift at an increasing rate against the number of dipoles in the line with the length of the line fixed, much like that of the ring structure. As the length is fixed, a greater number of dipoles means the dipoles are closer and each dipole interacts with more dipoles. Thus, the resultant interaction energy becomes greater, thereby causing a greater differential energy shift. Calculating the differential energy or frequency shift is critical to perform transitions along the Dicke ladder at specific frequencies in the presence of dipole-dipole interactions. As we have already discussed, this lays the foundation for the step-by-step Dicke state preparation using  $\pi$ -pulses. The calculations on differential energy shift will also be very important to study the effects of power broadening in our system of dipoles.

### 3.4 Power broadening

Now we will analyse the effect of power broadening for a linear arrangement of spins in case of  $\pi$ -pulse preparation of  $|J, 0\rangle$  state. Because the transition rate is the highest at the middle of the Dicke ladder, power broadening effects are enhanced there. Thus, in the following section, we carry out a simple calculation to get an idea of how power broadening effects may constrain the size of the spin ensemble as we consider the broadening at the last step, i.e.  $|J, -1\rangle \xrightarrow{\pi\text{-pulse}} |J, 0\rangle$ .

### 3.4.1 Calculating the maximum number of spins accounting for power broadening

In the study of atomic spectral transitions, the observed spectral lines are never infinitely narrow. In fact, there is always a finite thickness or width to them which is known as lifetime broadening [68] or power broadening. One of the factors behind this effect is the uncertainty of the energy states associated with the transition. Power broadening is a prevalent occurrence during emission and absorption processes. In our case, due to enhanced rates of transition near the middle of the Dicke ladder, the power broadening effects are also amplified. This raises concerns regarding the extent to which this can lead to the overlap of absorption spectra of transitions between different pairs of Dicke states and mask the frequency shifts induced by dipole-dipole interactions. This will hinder selective transition along the Dicke ladder. Here, we will compare the rate of excitation from  $|J, -J\rangle$  to  $|J, 0\rangle$  with the rate of decay from our  $|J, 0\rangle$  state, while ensuring the effective linewidth is lower than the differential frequency shift for  $|J, -1\rangle \rightarrow |J, 0\rangle$  to account for power broadening.

Our spins are symmetrical and are considered to act collectively. Hence, we can consider the ensemble of spins as a single big spin. We can write the Rabi frequency for the ensemble of spins for transition from  $|J, M-1\rangle$  to  $|J, M\rangle$  as  $\Omega_M = \Omega_s \langle J, M | J^+ | J, M-1 \rangle = \Omega_s \sqrt{(J-(M-1))(J+M)}$ , where  $\Omega_s$  is the single spin Rabi frequency. This means we can write the Rabi frequency for transition from  $|J, -1\rangle$  to  $|J, 0\rangle$  by just putting  $M = 0$  to obtain  $\Omega_0 = \Omega_s \sqrt{J(J+1)}$ . The decay rate of the spin ensemble can be written as  $\Gamma_M = \Gamma_s \langle J, M | J^+ J^- | J, M \rangle = \Gamma_s (J(J+1) - M(M-1))$ , where  $\Gamma_s$  is the single spin decay rate. So, we can express the decay rate from the Dicke state  $|J, 0\rangle$  by putting  $M = 0$  to obtain  $\Gamma_0 = \Gamma_s (J(J+1))$ . The effective linewidth of transition between Dicke states for the ensemble of spins is given by  $\gamma_{\text{eff}, M} = \Gamma_M \sqrt{1 + 2 \left( \frac{\Omega_M}{\Gamma_M} \right)^2}$ . The differential frequency shift between adjacent Dicke states is  $\delta_M = \langle J, M | V_{dd} | J, M \rangle - \langle J, M-1 | V_{dd} | J, M-1 \rangle$ . For a line of dipoles, the differential frequency shift is given as  $\delta_M = \left( \frac{4.8d^2}{r_0^3} \right) \left( \frac{1-2M}{2J-1} \right)$ . To prevent our frequency shifts from being masked by power broadening during transition, we require the effective linewidth to be less than the differential frequency shift, i.e.,

$$\gamma_{\text{eff}, M=0} < \delta_{M=0}$$

$$\Gamma_0 \sqrt{1 + 2 \left( \frac{\Omega_0}{\Gamma_0} \right)^2} < \left( \frac{4.8d^2}{r_0^3} \right) \left( \frac{1}{2J-1} \right) \quad (3.12)$$

We also want the duration of the pulse,  $\tau = \frac{\pi N}{2\Omega_0} = \frac{\pi}{2\Omega_0}$  needed to excite the system from ground Dicke

state  $|J, M = -J\rangle$  to  $|J, 0\rangle$  in  $N/2$  steps, to be much less than the decay time  $\frac{1}{\Gamma_0}$  from the transition.

$$\begin{aligned} \tau &<< \frac{1}{\Gamma_0} \\ \Omega_s \sqrt{J(J+1)} \frac{\pi}{2\Omega_0} &<< 1 \\ \frac{2\Omega_s}{\Gamma_s \pi \sqrt{J(J+1)}} &>> 1 \end{aligned} \tag{3.13}$$

We solve inequalities 3.12 and 3.13 simultaneously with  $J = N/2$  and obtain an upper bound for  $N < \left( \frac{19.2d^2}{\sqrt{2}\pi\Gamma_s r_0^3} \right)^{1/3}$ . For a specific case of  $\frac{d^2}{r_0^3} = 70$  kHz and  $\Gamma_s = 1$  kHz at  $r_0 = 10$ nm [69], we get  $N < 7$ . This is an important example to consider because the values are obtained from an actual experiment and therefore allows us to envision a real physical scenario where we will be limited in terms of scalability if we were to implement our  $\pi$ -pulse scheme. Thus, using strong dipole-dipole interactions to break the Dicke degeneracy and then applying selective transition to obtain the  $|J, 0\rangle$  state, accounting for power broadening only works for a limited number of spins. For larger number of spins, the broadening effects mask the differential frequency shift and the absorption spectra for transitions of different pairs of Dicke states overlap. Then it is no longer possible to cause discrete transition of our choice to reach arbitrary Dicke states. To avoid this constraint on the number of spins, we need to apply a method of state preparation that is scalable. We propose such a method in Chapter 4 where the fidelity of state preparation is high despite large number of spins in the system.

*"I confess, that very different  
from you, I do find sometimes  
scientific inspiration in mysti-  
cism ... but this is counterbal-  
anced by an immediate sense for  
mathematics."*

- Wolfgang Pauli

# 4

## Method 2: Dicke state preparation using Grover method

In this chapter we will investigate how to apply a Grover search method to prepare Dicke states. This method does not require selective addressing, dipole-dipole interactions or detunings. Although any Dicke state can be prepared by this method, our calculations largely focus on preparation of the  $|J, 0\rangle$  Dicke state. In this thesis we will mainly focus on the protocol of the Grover method and the physics behind its state preparation scheme. We will then briefly discuss its in-built robustness via dynamical decoupling and its application in quantum enhanced metrology. The results of implementing the Grover method in Dicke state preparation is discussed in details with a wider range of parameters and premises in the paper that I have co-authored [1].

## 4.1 Spin-cavity dynamics for geometric phase gates in Grover method

We start the chapter by discussing how the spin-cavity dynamics of our system gives rise to the dispersive coupling Hamiltonian, which leads up to the construction of the geometric phase gates (GPGs) that will be used in a Grover method to prepare the Dicke states.

### 4.1.1 Single spin-cavity dynamics

The bare Hamiltonian of the system is  $H_0 = \omega_0 J^z$ , taking  $\hbar = 1$ , and we will use a semi-classical field to drive the system, described by global rotations generated by the components of the collective angular momentum operator,  $J^x$  and  $J^y$  on the initial state. All the spins are equally coupled to a common quantized bosonic mode, characterised by the creation and annihilation operators for which the commutator  $[a, a^\dagger] = 1$  holds true. For this method to work, we do not need to be able to select any particular transition along the Dicke ladder which means unique transition frequency is not required. This also does not require the presence of dipole-dipole interactions. Thus, it is independent of the arrangement of the dipoles and works in systems that have weak coupling between the dipoles. The dipoles can be coupled to the external bosonic mode linearly or dispersively. In this chapter, we will analyse the case of dispersive coupling.

A possible physical system to implement the Grover method is a collection of Nitrogen-Vacancy ( $\text{NV}^-$ ) centres coupled to a cavity mode. The qubit can be encoded in the electronic sublevels of the  $\text{NV}^-$  centre,  $|0\rangle = |m = -1\rangle$  and  $|1\rangle = |m = 1\rangle$  as shown in the schematic in Figure 4.1 and the mode is characterised by the annihilation and creation operators,  $a$  and  $a^\dagger$  respectively. This is the effective two-level system, boxed in dashed red lines, which results from adiabatically eliminating the third sublevel,  $|m = 0\rangle$  by introducing the detunings  $\Delta_1$  and  $\Delta_{-1}$ . The coupling strength of both the detuned cavity transitions is  $g_c$ . The dynamics of this system can be described by the Hamiltonian,  $H$ .

$$\begin{aligned} H &= H_0 + g_c a e^{-i\omega_c t} |1\rangle \langle 0| + g_c a^\dagger e^{i\omega_c t} |0\rangle \langle 1| + g_c a e^{-i\omega_c t} |-1\rangle \langle 0| + g_c a^\dagger e^{i\omega_c t} |0\rangle \langle -1| \\ &= \omega_{0,1} |1\rangle \langle 1| + \omega_{0,-1} |-1\rangle \langle -1| + g_c a e^{-i\omega_c t} |1\rangle \langle 0| + g_c a^\dagger e^{i\omega_c t} |0\rangle \langle 1| + g_c a e^{-i\omega_c t} |-1\rangle \langle 0| + g_c a^\dagger e^{i\omega_c t} |0\rangle \langle -1| \end{aligned} \quad (4.1)$$

We can express this Hamiltonian in the interaction picture as  $H_I$ .

$$H_I = g_c a e^{-i(\omega_c - \omega_{0,1})t} |1\rangle \langle 0| + g_c a^\dagger e^{i(\omega_c - \omega_{0,1})t} |0\rangle \langle 1| + g_c a e^{-i(\omega_c - \omega_{0,-1})t} |-1\rangle \langle 0| + g_c a^\dagger e^{i(\omega_c - \omega_{0,-1})t} |0\rangle \langle -1| \quad (4.2)$$

To obtain an effective Hamiltonian which essentially gets rid of the rapidly oscillating terms due to time averaging, we make use of the effective Hamiltonian theory as described in [70] and we write the interaction Hamiltonian,  $H_I$  in the form

$$H_I = h_1 e^{-i\Delta_1 t} + h_2 e^{-i\Delta_2 t} + h_1^\dagger e^{i\Delta_1 t} + h_2^\dagger e^{i\Delta_2 t}, \quad (4.3)$$

where  $\Delta_1 = \omega_c - \omega_{0,1}$ ,  $\Delta_2 = \omega_c - \omega_{0,-1}$ ,  $h_1 = g_c a |1\rangle \langle 0|$  and  $h_2 = g_c a |-1\rangle \langle 0|$ . Now, we can directly calculate the effective Hamiltonian,  $V'_{\text{eff}}$  using the formula [70]

$$\begin{aligned} V'_{\text{eff}} &= \sum_{m,n=1}^2 \frac{1}{\delta_{m,n}} [h_m^\dagger, h_n] e^{i(\delta_m - \delta_n)t} \\ &= \frac{1}{\delta_{1,1}} [h_1^\dagger, h_1] + \frac{1}{\delta_{2,2}} [h_2^\dagger, h_2] + \frac{1}{\delta_{1,2}} [h_1^\dagger, h_2] e^{i(\delta_1 - \delta_2)t} + \frac{1}{\delta_{2,1}} [h_2^\dagger, h_1] e^{i(\delta_2 - \delta_1)t} \end{aligned} \quad (4.4)$$

where we used  $\frac{1}{\delta_{m,n}} = \frac{1}{2}(\frac{1}{\delta_m} + \frac{1}{\delta_n})$  and for our particular case,  $\delta_1 = \Delta_1$ ,  $\delta_2 = \Delta_{-1}$  and  $h_1$  and  $h_2$  are as expressed previously. Substituting these and using the cavity mode bosonic commutator  $[a, a^\dagger] = 1$ , we get

$$\begin{aligned} V'_{\text{eff}} &= \frac{g_c^2}{\Delta_1} [ |0\rangle \langle 1| a^\dagger, a |1\rangle \langle 0| ] + \frac{g_c^2}{\Delta_{-1}} [ |0\rangle \langle -1| a^\dagger, a |-1\rangle \langle 0| ] \\ &+ \frac{g_c^2}{\Delta_{1,-1}} [ |0\rangle \langle 1| a^\dagger, a |-1\rangle \langle 0| ] e^{i(\Delta_1 - \Delta_{-1})t} + \frac{g_c^2}{\Delta_{-1,1}} [ |0\rangle \langle -1| a^\dagger, a |1\rangle \langle 0| ] e^{i(\Delta_{-1} - \Delta_1)t} \\ &= \frac{g_c^2}{\Delta_1} (-a^\dagger a |1\rangle \langle 1| + a a^\dagger |0\rangle \langle 0|) + \frac{g_c^2}{\Delta_{-1}} (a^\dagger a |0\rangle \langle 0| - a a^\dagger |-1\rangle \langle -1|) \\ &+ \frac{g_c^2}{\Delta_{1,-1}} e^{i(\Delta_1 - \Delta_{-1})t} (-a a^\dagger |-1\rangle \langle 1|) + \frac{g_c^2}{\Delta_{-1,1}} e^{i(\Delta_{-1} - \Delta_1)t} (-a a^\dagger |1\rangle \langle -1|) \\ &= \frac{g_c^2}{\Delta_1} (-a^\dagger a |1\rangle \langle 1| - |1\rangle \langle 1| + a^\dagger a |0\rangle \langle 0|) \\ &+ \frac{g_c^2}{\Delta_{-1}} (a a^\dagger (|0\rangle \langle 0| - a^\dagger a |-1\rangle \langle -1| - |1\rangle \langle 1|) \\ &= -g_c^2 \left( \frac{(a^\dagger a + 1) |1\rangle \langle 1|}{\Delta_1} + \frac{(a^\dagger a + 1) |-1\rangle \langle -1|}{\Delta_{-1}} \right) \\ &= -g_c^2 \left( \frac{a^\dagger a + 1}{2} \right) \left( \frac{1}{\Delta_1} - \frac{1}{\Delta_{-1}} \right) \sigma_z - g_c^2 \left( \frac{a^\dagger a + 1}{2} \right) \left( \frac{1}{\Delta_1} - \frac{1}{\Delta_{-1}} \right) (|1\rangle \langle 1| + |-1\rangle \langle -1|), \end{aligned} \quad (4.5)$$

where we note that when  $\Delta_{-1} \gg \Delta_1$ , the terms with  $e^{i(\Delta_1 - \Delta_{-1})t}$  and  $e^{i(\Delta_{-1} - \Delta_1)t}$  become 0 and we get the relevant dispersive part of the above Hamiltonian as  $V_{\text{eff}} = \frac{1}{2} \left( \frac{g_c^2}{\Delta_1} - \frac{g_c^2}{\Delta_{-1}} \right) \sigma_z a^\dagger a = \kappa \sigma_z a^\dagger a$ , where we have written  $\kappa = \frac{1}{2} \left( \frac{g_c^2}{\Delta_1} - \frac{g_c^2}{\Delta_{-1}} \right)$ . This is our effective dispersive Hamiltonian.

### 4.1.2 Multiple spin-cavity dynamics

Now, let us consider  $n$  spins in the cavity and assume that the cavity mode wavelength,  $\lambda$  is much greater than the separation,  $|\Delta\vec{r}|$  between the spins, i.e.,  $\lambda \gg |\Delta\vec{r}|$ . This means that all the spins see the same cavity field and are indistinguishable. So, we can write the interaction Hamiltonian,  $V_{c,n}$  of this collection of indistinguishable spins just by substituting for the collective angular momentum operator,  $J^z$  defined as  $J^z = \frac{1}{2} \sum_{j=1}^n \sigma_j^z$  in the expression for  $V_{\text{eff}}$ .

$$V_{c,n} = \kappa J^z a^\dagger a, \quad (4.6)$$

There are two important cavity mode operators to consider [71]. The first is the displacement operator,  $D(\alpha) = e^{\alpha a^\dagger - \alpha^* a}$  and the second is the rotation operator,  $R(\theta) = e^{i\theta a^\dagger a}$ . These operators obey the following relations.

$$D(\beta)D(\alpha) = e^{i\text{Im}[\beta\alpha^*]} D(\alpha + \beta) \quad (4.7)$$

$$R(\theta)D(\alpha)R(-\theta) = D(\alpha e^{i\theta}) \quad (4.8)$$

$$D(\alpha e^{i\theta C}) = R(\theta C)D(\alpha)R(-\theta C), \quad (4.9)$$

where  $R(\theta C) = e^{i\theta C \otimes a^\dagger a}$  and  $C$  is any operator acting on a system other than the cavity.



### 4.1.3 Geometric phase gates

We can derive the expression for our geometric phase gate,  $U_{\text{gpg}}$  which is the following sequence of the displacement and rotation operators, using the relations 4.7, 4.8 and 4.9.

$$\begin{aligned}
U_{\text{gpg}} &= D(-\beta)R(\theta C)D(-\alpha)R(-\theta C)D(\beta)R(\theta C)D(\alpha)R(-\theta C) \\
&= D(-\beta)D(-\alpha e^{i\theta C})D(\beta)D(\alpha e^{i\theta C}) \\
&= e^{i \text{Im}[\beta \alpha^* e^{-i\theta C}]} D(-\alpha e^{i\theta C} - \beta) e^{i \text{Im}[\beta \alpha^* e^{-i\theta C}]} D(\alpha e^{i\theta C} + \beta) \\
&= e^{i2 \text{Im}[\beta \alpha^* e^{-i\theta C}]} D(-\alpha e^{i\theta C} - \beta) D(\alpha e^{i\theta C} + \beta) \\
&= e^{i2 \text{Im}[\beta \alpha^* e^{-i\theta C}]} e^{i \text{Im}[(-\alpha e^{i\theta C} - \beta)(-\alpha e^{i\theta C} - \beta)]} D(-\alpha e^{i\theta C} - \beta + \alpha e^{i\theta C} + \beta) \\
&= e^{i2 \text{Im}[\beta \alpha^* e^{-i\theta C} - (1/2)\alpha \alpha^* - (1/2)\alpha \beta^* e^{-i\theta C} - (1/2)\beta \alpha^* e^{-i\theta C} - (1/2)\beta \beta^*]} \\
&= e^{i2 \text{Im}[(1/2)\beta \alpha^* e^{-i\theta C} - (1/2)\alpha \beta^* e^{i\theta C} - (1/2)|\alpha|^2 - (1/2)|\beta|^2]} \\
&= e^{i2 \text{Im}[(1/2)|\alpha \beta| e^{-i\phi} e^{-i\theta C} - (1/2)|\alpha \beta| e^{i\phi} e^{i\theta C} - (1/2)|\alpha|^2 - (1/2)|\beta|^2]} \\
&= e^{2i|\alpha \beta| \text{Im}[(1/2)e^{-i\phi - \theta C} - (1/2)e^{i\phi + \theta C} - (1/2)|\alpha|^2 - (1/2)|\beta|^2]} \\
&= e^{i2|\alpha \beta| \text{Im}[i \sin(\phi + \theta C) - (1/2)|\alpha|^2 - (1/2)|\beta|^2]} \\
&= e^{-2i|\alpha \beta| \sin(\theta C + \phi)}
\end{aligned} \tag{4.10}$$

where we also used the relations  $e^{i\theta C} e^{i\theta C} = e^{2i\theta C}$ ,  $e^{i\theta C} e^{-i\theta C} = 1$ , as  $[C, C] = 0$ ,  $[D(-\alpha e^{i\theta C} - \beta), e^{i \text{Im}[\beta \alpha^* e^{-i\theta C}]}] = 0$ ,  $\alpha = |\alpha| e^{i\phi_\alpha}$ ,  $\alpha \beta^* = |\alpha| e^{i\phi_\alpha} |\beta| e^{-i\phi_\beta} = |\alpha \beta| e^{i(\phi_\alpha - \phi_\beta)} = |\alpha \beta| e^{i\phi}$ , with  $\phi = (\phi_\alpha - \phi_\beta)$ ,  $e^{i\theta C} = \mathbb{1} + (i\theta C) + \frac{1}{2!}(i\theta C)^2 + \frac{1}{3!}(i\theta C)^3 + \dots$ ,  $\sin(\theta C) = \theta C - \frac{1}{3!}(\theta C)^3 + \frac{1}{5!}(\theta C)^5 - \dots$ ,  $e^{i\theta C} - e^{-i\theta C} = 2i \sin(\theta C)$ . We can view  $U_{\text{gpg}}$  in phase space of the cavity mode as shown in Figure 4.2. Since we are using dispersive coupling of spins to the cavity mode, our rotation operator will involve the dispersive Hamiltonian,  $V_{c,n}$  with  $J^z$  operator. By letting  $C = J^z$  and  $\theta = \kappa\tau$ , where  $\tau$  is the time of interaction, we obtain  $e^{-iV_{c,n}\tau} = R(-\theta C) = R(-\theta J^z)$ . Both  $R(-\theta J^z)$  and  $R(\theta J^z)$  are needed for evolution of the GPG and it can be done by using global flips involving  $J^x$  as  $R(\theta J^z) = e^{-i\pi J^x} R(-\theta J^z) e^{i\pi J^x}$ . The spins decouple from the mode at the end of the GPG loop. If the cavity begins in the vacuum state then the first  $R(-\theta J^z)$  is unnecessary. Thus, in total, we need three interactions generated by  $V_{c,n}$ . However, we can include the first operation  $R(-\theta J^z)$  because it can act to cancel total free evolution by commuting with the bare Hamiltonian  $H_0$  and subdue dephasing errors. We can adjust  $\theta$  by adjusting  $\tau$ . Now, let us assume an even number of spins, although the scheme can be amended to suit odd numbers of spins as well, and consider a sequence,  $Y = U_{n/2} \dots U_1$  of geometric phase gates,  $U_{k,l} = e^{-i2|\alpha \beta| \sin(\theta_k C + \phi_k(l))}$  with  $k$  ranging from 1 to  $n/2$  and  $l$  from 0 to  $n$ . So,

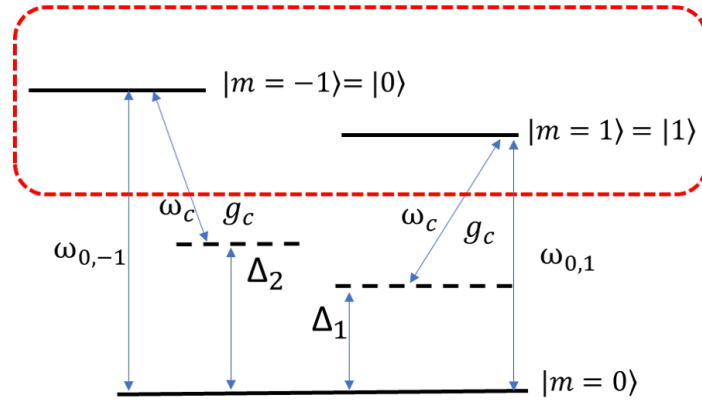


Figure 4.1: NV states as a qubit.

we can express  $Y$  as

$$Y(l) = \sum_{M=-J}^J e^{-i2|\alpha\beta| \sum_{k=1}^{n/2} \sin(\theta_k M + \phi_k(l))} |J, M\rangle \langle J, M| \quad (4.11)$$

We pick  $\phi_k(l) = \frac{2\pi k}{n+1}(J-l) + \frac{\pi}{2}$ ,  $\theta_k = \frac{2\pi k}{n+1}$  and  $|\alpha\beta| = \frac{\pi}{n+1}$ . Then, by the following relations, we will confirm  $Y$ .

Sine-cosine complementary angles:  $\sin(\theta_k M + \phi_k(l))$

$$\begin{aligned} &= \sin\left(\frac{2\pi k}{n+1}M + \frac{2\pi k}{n+1}(J-l) + \frac{\pi}{2}\right) \\ &= \cos\left(\frac{2\pi k}{n+1}(M+J-l)\right) \end{aligned} \quad (4.12)$$

$$\text{Fourier cosine series analysis: } \frac{2}{n+1} \sum_{k=1}^{n/2} \cos\left(\frac{2\pi k(M+J-l)}{n+1}\right) = \delta_{l, M+J} - \frac{1}{n+1} \quad (4.13)$$

Thus, we get  $Y(l)$  in terms of a projector operator of collective states with  $l$  number of excited spins,  $|J, M = l - J\rangle$ , i.e.  $Y(l) = e^{-i\pi|J, l-J\rangle\langle J, l-J|}$  up to a global phase. So, now, we have a way to apply a tunable phase, which is a  $\pi$  phase shift here, to states  $|J, M\rangle \langle J, M|$  where  $M = -J, \dots, +J$ . We will use  $Y(l)$  to construct operators for Grover iterations in section 4.2. In addition to the collective angular momentum operators,  $J^x$  and  $J^y$ , now we have access to a control algebra,  $a = \{J^x, J^y, |J, M\rangle \langle J, M|\}$ . Therefore, we can perform any unitary over the state space  $\{|J, M\rangle\}_{M=-J}^J$  and find a sequence of gates to perform the state mapping  $|J, -J\rangle \rightarrow |J, 0\rangle$ , where  $|J, 0\rangle$  is our target Dicke state.

## 4.2 Details of our Grover method

Our initial state,  $|s\rangle = e^{iJ^y\pi/2} |J, -J\rangle$  is prepared by applying  $J^y$  rotation on the ground collective state  $|J, -J\rangle$ . We want to apply Grover iterations to this state to obtain target state,  $|w\rangle = |J, 0\rangle$ . We use two

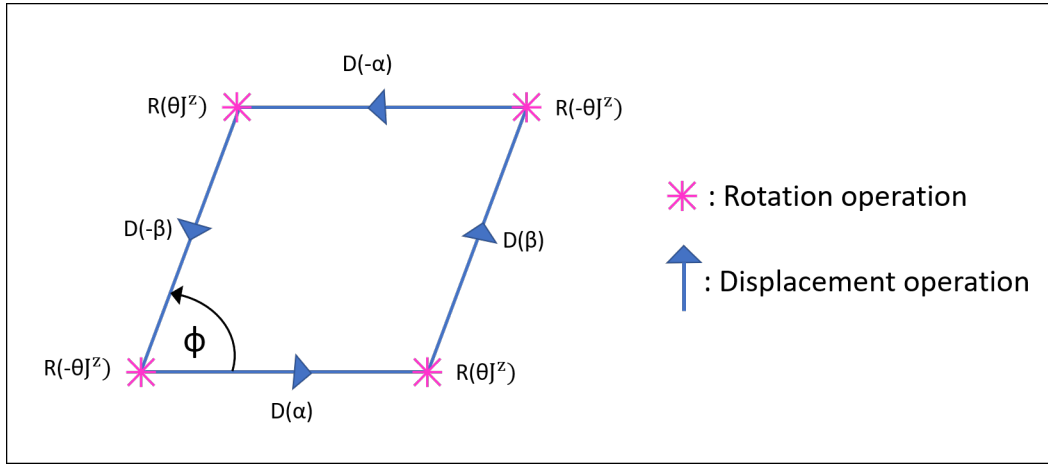


Figure 4.2: Closed loop formed by one geometric phase gate.

operators,  $U_s$  and  $U_w$  to construct the Grover iterations. Using  $Y(0)$  from equation 4.11 which puts a  $\pi$  phase shift on the ground Dicke state we obtain operator  $U_s = e^{-i\pi|s\rangle\langle s|} = e^{iJ^y\pi/2}Y(0)e^{-iJ^y\pi/2} = e^{iJ^y\pi/2}e^{i\pi|J,-J\rangle\langle J,-J|}e^{-iJ^y\pi/2}$ . Similarly, we can derive an expression corresponding to the target  $|J,0\rangle$  state to construct operator  $U_w = Y(n/2) = e^{-i\pi|w\rangle\langle w|} = e^{-i\pi|J,0\rangle\langle J,0|}$ . The initial and target states are not orthonormal. So, we write an orthonormal basis so that  $\langle s'|w\rangle = 0$ , where,  $|s'\rangle = \frac{|s\rangle - |w\rangle\langle w|s\rangle}{\sqrt{1 - |\langle w|s\rangle|^2}}$ . The state  $|s\rangle$  is geometrically rotated by an angle  $\frac{\delta}{2}$  from the state  $|s'\rangle$  as shown in Figure 4.3. Here,  $\delta$  is defined as  $\sin \frac{\delta}{2} = \langle w|s\rangle$ . A single Grover step,  $G$  is constructed by successive application of operators  $U_s$  and  $U_w$ , i.e.  $G = U_s U_w$ . This rotates the initial state  $|s\rangle$  by angle  $\delta$  towards the target state  $|w\rangle$  as shown in Figure 4.3. The operator  $U_w$  is a reflection along  $|s'\rangle$  and operator  $U_s$  is a reflection along  $|s\rangle$ . Thus, the state vector is contained within the plane spanned by  $|w\rangle$  and  $|s'\rangle$  after every time  $U_w$  and  $U_s$  are applied. So, a single Grover iteration induces a rotation of  $\delta$  on the initial state  $|s\rangle$ . We should stop when the state vector reaches as close as possible to the target state without going past it. We can calculate the overlap,  $\langle w|s\rangle$  of the initial and target states by using the Wigner (small) d-matrix elements to check how close the initial state has come to the target state. In general, the d-matrix element of the  $j$ th irreducible representation or irrep,  $d_{M',M}^J$  is given as [66] :

$$\begin{aligned}
 \langle w|s\rangle &= \langle J, M'| e^{-iJ^y\beta} |J, M\rangle \\
 &= d_{M',M}^J(\beta) \\
 &= \sum_{M=-J}^J \left( \sum_{k=-J}^J (-1)^{k-M+M'} \frac{\sqrt{(J+M)!(J-M)!(J+M')!(J-M')!}}{(M+J-k)!k!(J-k-M')!(k-M+M')!} \right. \\
 &\quad \left. \cos^{2J+2k+M-M'} \left( \frac{\beta}{2} \right) \sin^{2k-M+M'} \left( \frac{\beta}{2} \right) \right)
 \end{aligned} \tag{4.14}$$

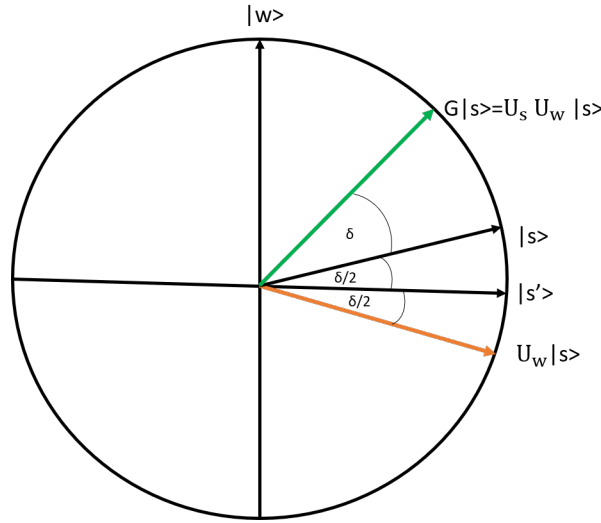


Figure 4.3: Geometric interpretation of application of Grover method to the initial state.

In our case, the Euler angle of rotation is  $\beta = \frac{-\pi}{2}$ , and the total angular momentum projections for the states are  $M = -J$  and  $M' = 0$ . Putting these values into the above expression, summing over  $k$  so that the factorials are non-negative and simplifying, we get the overlap between our initial and target states as:

$$\begin{aligned}
 \langle w | s \rangle &= \langle J, M' = 0 | e^{iJ^y \pi/2} | J, M = -J \rangle \\
 &= d_{0, -J}^J \left( \frac{-\pi}{2} \right) \\
 &= \frac{2^{-J} \sqrt{(2J)!}}{J!}
 \end{aligned} \tag{4.15}$$

A further simplification can be done for  $J \gg 1$ , using Stirling's approximation  $x! \approx x^x e^{-x} \sqrt{2\pi x}$ , to give  $\langle w | s \rangle \approx \frac{1}{(\pi J)^{1/4}} = \frac{1}{(\pi \frac{n}{2})^{1/4}}$ , as  $J = \frac{n}{2}$ . We can now use this expression to find the optimal number of Grover iterations,  $T$  for the earliest time that we can reach the target state starting from the initial state.

$$T = \left\lfloor \frac{\pi}{4|\langle w | s \rangle|} \right\rfloor = \left\lfloor \frac{\pi^{5/4} n^{1/4}}{2^{9/4}} \right\rfloor \tag{4.16}$$

At this time, the fidelity overlap,  $F$  for  $n \gg 1$  is given as:

$$F = |\langle w | G^T | s \rangle|^2 = \sin^2\left(\left(T + \frac{1}{2}\right)\delta\right) > 1 - \sqrt{\frac{2}{\pi n}} \tag{4.17}$$

We note that the fidelity error which is given by  $F_{\text{error}} = 1 - F$  falls proportionally to  $\sqrt{\frac{2}{\pi n}}$  when  $n \gg 1$ . There can be further decrease in fidelity error if the floor function for  $T$  is around half integer. Some fidelity error values,  $F_{\text{error}}$  for our protocol are  $1.84 \times 10^{-4}$ ,  $1.57 \times 10^{-5}$ ,  $1.68 \times 10^{-6}$ ,  $3.65 \times 10^{-8}$ ,  $1.92 \times 10^{-8}$  for number of spins,  $n = 10, 70, 260, 700, 1552$  respectively. These are high fidelities that increase with the number of spins if we ignore noise, thereby implying our scheme may be scalable to larger spin numbers than other existing Dicke state preparation schemes.

## 4.3 Decoherence effects

There will be two main types of losses in our cavity-spin system during the Grover operations that lowers the fidelity overlap. The first is the decay of the bosonic cavity mode and the second is the loss of coherence of spins, also known as dephasing. We will discuss how the built-in dynamical decoupling, based on the spin echo technique, of our Grover method suppresses decoherence effects.

### 4.3.1 Bosonic mode damping

We consider the cavity mode as an open quantum system, where loss occurs at the rate of  $\gamma_{\text{cav}}$ . At first the mode and the spins are entangled but they decouple at the end of the GPG iteration. We need to change the third and fourth displacement operations to  $D(-\alpha e^{-\gamma_{\text{cav}}\theta_k/\kappa})$  and  $D(-\beta e^{-\gamma_{\text{cav}}\theta_k/\kappa})$  to disentangle the spins and the cavity. The input Dicke state can be written as the density operator,  $\rho_{\text{in}} = \sum_{M,M'} \rho_{M,M'} |J, M\rangle \langle J, M'|$ . By incorporating decay, the process for the  $k$ th GPG can be represented by a map,  $\mathcal{E}^{(k)}$  given by [72]

$$\mathcal{E}^{(k)}(\rho_{\text{in}}) = U_{\text{gpg}}(\theta_k, \phi_k, \chi) \left[ \sum_{M,M'} R_{M,M'}^{(k)} \rho_{M,M'} |J, M\rangle \langle J, M'| \right] U_{\text{gpg}}^\dagger(\theta_k, \phi_k, \chi), \quad (4.18)$$

where  $R^{(k)}$  is a global dephasing map and we set  $|\alpha\beta| = \chi$  in the expression for  $U_{\text{gpg}}$ . This single process fidelity is given by [72]:

$$F_{\text{pro}}^{(k)} = \frac{1}{(n+1)^2} \sum_{M,M'} \text{Re}[R_{M,M'}^{(k)}]. \quad (4.19)$$

An important lower bound for the fidelity is  $F_{\text{pro}}^{(k)} > 1 - \frac{4\pi^2\gamma_{\text{cav}}/\kappa}{(n+1)(e^{-3\gamma_{\text{cav}}\theta_k/2\kappa} + e^{-\gamma_{\text{cav}}\theta_k/2\kappa})}$ . This is useful because it gives the value of our worst possible fidelity for the gate implementation. Then the total fidelity is calculated by the concatenation of  $Tn$  GPGs with the average action angle assumed to be  $\theta_{\text{avg}} = \frac{\sum_k \theta_k}{n/2} = \frac{3\pi}{5}$  to give  $F_{\text{pro}} > (1 - 2\pi^2\gamma_{\text{cav}}/\kappa)^T$ . The total fidelity falls off proportionally to  $n^{\frac{1}{4}}$  for  $\frac{\gamma_{\text{cav}}}{\kappa} \ll 1$ , i.e. when the decay rate of the cavity is much smaller relative to the coupling strength.

### 4.3.2 Dephasing and its suppression by dynamical decoupling

Dephasing refers to the loss of coherence of the spins inside the cavity. This is a purely quantum mechanical effect during which the system loses its coherent behaviour as the spins couple to the environmental degrees of freedom. This phenomenon also degrades the fidelity for the GPG implementation in our system. The spins themselves can undergo two types of damping. The first is

amplitude damping owing to spin relaxation and the second is phase damping or dephasing. We assume that we choose qubit states that have very long relaxation times compared to decoherence time so as to minimise amplitude damping. This can occur because of selection rules or due to the transition frequency of the spins being detuned considerably away from the fast spin exchange transition frequency. The target state can be upconverted to states that are sensitive to spin-flips. Due to the cyclic nature of the evolution of the GPGs there will be some intrinsic fault tolerance. Spin flip pulses between dispersive gates can be used to cancel the environmental noise to low order. This effect is called dynamical decoupling. It is a technique to negate the effects of environmental noise by using a series of spin-flip pulses which will on-average neutralize the system-environment coupling. The idea is derived from the spin echo effect or Hahn echo effect [73, 74], where a  $\pi$ -pulse is applied to flip the spins after a duration  $t$  of dephasing. The dephasing process is an inhomogeneous spreading of spin polarisations which cause some spins to slow down and some to speed up, resulting in decay of coherence. Due to the inversion pulse, after time  $2t$ , the inhomogeneous spreading causes the flipped spins to refocus with only a  $\pi$ -phase shift. Thus, the net effect is the cancellation of noise due to the inhomogeneous dephasing as shown in Figure 4.4, where spin  $c$  is spreading out at the fastest speed, then  $b$  and the slowest is  $a$ . After the reversion pulse that causes an instantaneous flip, the faster spins catch up to the slower spins, resulting in the merge. In our case, a further flip is applied to the spins and they regain their original direction. Here, we discuss global dephasing of the spins which is the most prominent source of noise for our system, whereby unlike local dephasing, the states are not mixed with lower  $J$ -subspaces outside the Dicke subspace. We consider dispersive coupling of spins to a bath of oscillators described by Hamiltonian,  $H = H_E + H_{SE}$  where the Hamiltonian of the bath or environment,  $H_E$  and the Hamiltonian of system-bath interaction,  $H_{SE}$  satisfy the commutation relation  $[b_i, b_k^\dagger] = \delta_{j,k}$  and are given as

$$H_E = \sum_k \omega_k b_k^\dagger b_k, \quad H_{SE} = \sum_k J^z (b_k g_k^* + b_k^\dagger g_k), \quad (4.20)$$

Considering evolution for either  $U_s$  or  $U_w$  operator, dephasing implies that the coherence terms of the density matrix,  $\rho_{M,M'}(T_d)$  of the system after time,  $T_d$  falls off as

$$\rho_{M,M'}(T_d) = \rho_{M,M'}(0) e^{-(M-M')^2 \Gamma_{\text{eff}}(T_d)} \quad (4.21)$$

For Gaussian bath statistics, effective dephasing rate in 4.21 can be expressed in terms of the spectral noise,  $S(\omega)$  and filter function,  $f(\omega)$  [75].

$$\Gamma_{\text{eff}}(T_d) = \frac{1}{2\pi} \int_0^\infty d\omega S(\omega) |f(\omega)|^2, \quad (4.22)$$

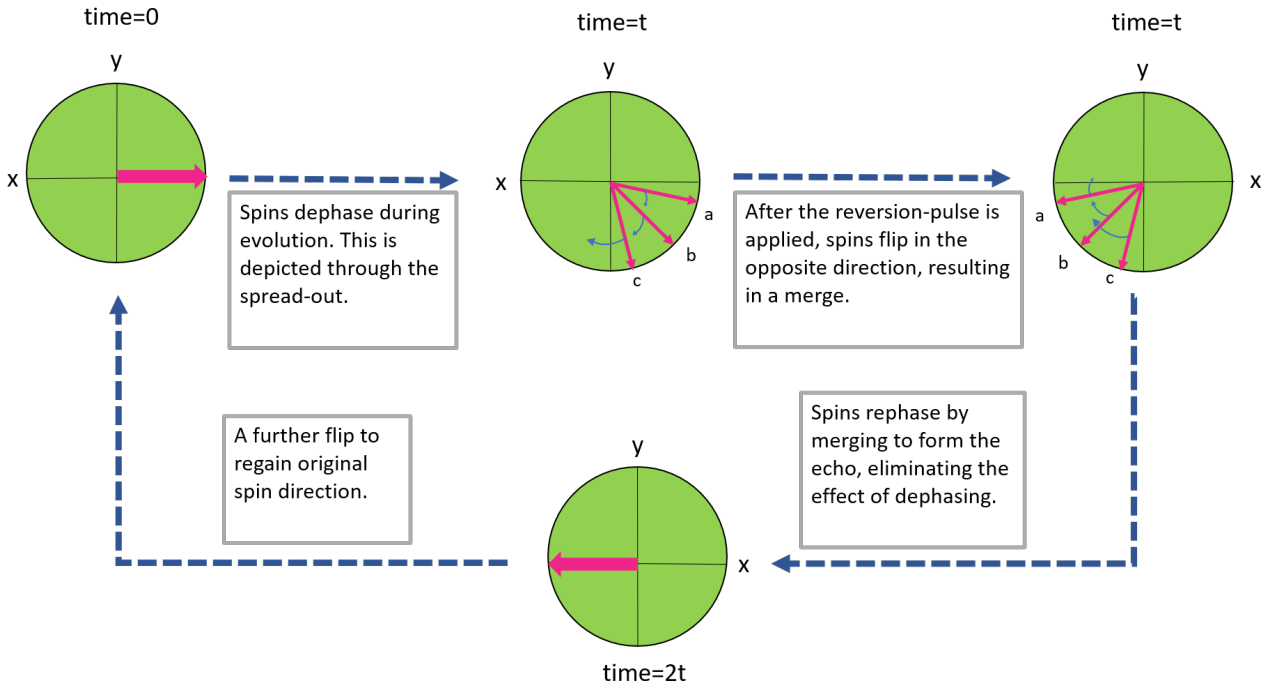


Figure 4.4: Spin echo effect that eliminates the effect of dephasing.

where the filter function,  $f(\omega)$  is the Fourier transform of the time dependent control pulse sequence,  $F(t)$  which is a unit function that switches its sign corresponding to every collective spin flip expressed as

$$F(t) = \begin{cases} 1 & t \in \bigcup_{k=1}^{n/2} \{[T_k^{(0)}, T_k^{(1)}] \cup [T_k^{(2)}, T_k^{(3)}]\} \\ -1 & t \in \bigcup_{k=1}^{n/2} \{[T_k^{(1)}, T_k^{(2)}] \cup [T_k^{(3)}, T_k^{(4)}]\} \\ 0 & \text{otherwise} \end{cases}$$

where  $T_k^{(m)}$  are the flip times. The filter function can be explicitly written as

$$|f(\omega)|^2 = \frac{1}{\omega^2} \left| \sum_{k=1}^{n/2} (e^{i\omega T_k^{(0)}} - 2e^{i\omega T_k^{(1)}} + 2e^{i\omega T_k^{(2)}} - 2e^{i\omega T_k^{(3)}} + e^{i\omega T_k^{(4)}}) \right|^2 \quad (4.23)$$

This filter function can be expanded in a Taylor series in  $\omega/\kappa$  and the lowest order expansion terms extracted to give a useful measure of the dephasing rate,  $\kappa^2 |f(\omega)|^2$ .

$$\kappa^2 |f(\omega)|^2 \approx \frac{(\omega/\kappa)^2 \pi^4 n^2 (n+2)^2}{9(n+1)^2}. \quad (4.24)$$

To realize the advantage of dynamical decoupling we can calculate the dephasing reduction factor,  $\frac{|f(\omega)|^2}{|f^{(0)}(\omega)|^2}$  which is a ratio of the dephasing rate with dynamical decoupling to dephasing rate without dynamical decoupling. This ratio shows the extent to which the overall dephasing rate has been suppressed on account of dynamical decoupling. We consider two regions of interest for this reduction

factor, assuming flat noise spectral statistics. Firstly, for  $\omega/\kappa < 1/\pi n$ ,  $\frac{|f(\omega)|^2}{|f^{(0)}(\omega)|^2} = \pi^2 \omega^2 / \kappa^2$ . Secondly, for  $1/\pi n < \omega/\kappa < 1/2$ , the reduction factor is approximately  $\frac{|f(\omega)|^2}{|f^{(0)}(\omega)|^2} \approx 0.22$ . Thus, the spins experience much smaller dephasing in the presence of dynamical decoupling which enables our scheme to attain higher fidelities. Details of dynamical suppression of dephasing can be found in our paper [1]. It should be noted that it is possible to reach even lower reduction factors by searching for optimal sequences of our GPGs.

## 4.4 Quantum metrology using Dicke states

A core task of metrology is uncertainty calculation of a phase parameter,  $\nu$  which is estimated by measuring an observable  $X$  on the final state after preparation. The phase parameter is associated with the unitary evolution,  $U(\nu) = e^{-i\nu J^y}$  that describes the collective rotation,  $J^y$  by application of a field such as a magnetic field of strength,  $\nu$  on a spin ensemble. The uncertainty is expressed as a variance,  $(\Delta\nu)^2$  of the phase parameter.

$$(\Delta\nu)^2 = \frac{(\Delta X(\nu))^2}{|\partial_\nu \langle X(\nu) \rangle|^2}. \quad (4.25)$$

The lower the variance, the higher the precision of parameter estimation. Thus, the goal in metrological tasks is to lower this variance. However, there is a lower bound on this called the Cramér-Rao bound [76] which is the least possible uncertainty that can be obtained among all the observables that can be chosen for measurement. If we choose  $X = J^{z2}$  as our observable, the variance is given by [77]

$$(\Delta\nu)^2 = ((\Delta J^{x2})^2 f(\nu) + 4\langle J^{x2} \rangle - 3\langle J^{y2} \rangle - 2\langle J^{z2} \rangle (1 + \langle J^{x2} \rangle) + 6\langle J^z J^{x2} J^z \rangle) (4(\langle J^{x2} \rangle - \langle J^{z2} \rangle)^2)^{-1}, \quad (4.26)$$

where  $f(\nu) = \frac{(\Delta J^{z2})^2}{(\Delta J^{x2})^2 \tan^2(\nu)} + \tan^2(\nu)$ . For our choice of prepared state in this chapter, i.e. the superabsorptive Dicke state  $|J, 0\rangle$ , the variance is minimum when  $\nu = 0$  and the Cramér-Rao bound saturated, i.e Cramér-Rao equality is achieved as  $(\Delta\nu)^2 = \frac{2}{n(n+2)}$ , where  $n$  is the number of spins. Thus, the uncertainty,  $\Delta\nu = \frac{\sqrt{2}}{\sqrt{n(n+2)}}$  scales as  $1/n$  which is characteristic of the Heisenberg precision scaling in metrology. To check the efficiency of our Grover method to prepare Dicke state, we calculated the uncertainty for its use in metrology for  $n = 10$  spins after  $|J, 0\rangle$  preparation while taking into account mode decay characterised by decay rate,  $\gamma_{\text{cav}}$  and global dephasing characterised by dephasing rate,  $\Gamma_{\text{eff}}$ . Figure 4.5 shows how the uncertainty increases with increasing mode decay and increasing dephasing values. For  $\gamma_{\text{cav}}/\kappa \lesssim 0.01$  we overcome the shot noise limit. Furthermore, in the absence of decay, the uncertainty,  $(\Delta\nu)^2 = 0.138$  is close to the Cramér-Rao bound of  $(\Delta\nu)^2 = 0.129$ . In



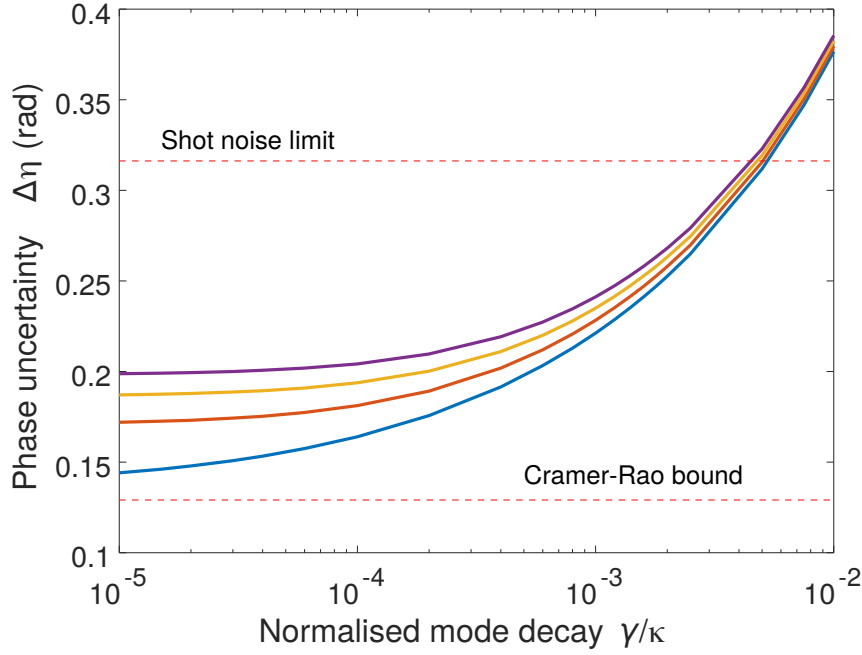


Figure 4.5: Phase uncertainty vs normalised mode decay for different values of  $\Gamma_{\text{eff}}/\kappa = 0$  (light blue),  $0.5 \times 10^{-3}$  (red),  $1.0 \times 10^{-3}$  (yellow),  $1.5 \times 10^{-3}$  (purple). This plot was produced by Dr Mattias Johnsson [1].

order to calculate value of  $\langle J^{z2} \rangle$ , we can measure the observable  $J^z$  in suitable experiments, square the outcome of the individual measurements, repeat the measurements and take the average.

## 4.5 Implementation

The Grover method discussed here is a versatile scheme. It can be customized to different types of physical systems which involve collective dispersive couplings of spins to oscillators. Some examples of such systems are Rydberg atoms dispersively interacting to a microwave cavity [78, 79], superconducting artificial atom coupled to microwave resonator using strong dispersive interaction [80], architectures with coupling between trapped ions and optical cavity modes [81] or motional cavity modes [82]. More examples include the Nitrogen Vacancy (NV) defect centres in diamonds coupled to microwave cavity mode inside a superconducting transmission line resonator [83].



*"If we want to solve a problem  
that we have never solved before,  
we must leave the door to the  
unknown ajar."*

- Richard P. Feynman

# 5

## Method 3: Dicke state preparation using optimal control techniques

In this chapter we will describe the third method to prepare Dicke states. In this case, the spins are coupled linearly to a common bosonic mode of cavity and the induced interaction of spins and the cavity mode is non-linear. We analyse the fidelity of our state preparation using a global rotation on the spins and a quadratic spin interaction. We optimise for the control pulse sequence required to achieve it by implementing numerical optimal control techniques in the QuTip package called Qtrl.

### 5.1 Spin-cavity dynamics for optimal control method

So far in this thesis, we have explored two methods to prepare Dicke states. In the first approach we broke the linear energy spacing of the Dicke ladder via dipole-dipole interactions. In the second procedure we considered highly non-linear gates induced via dispersive coupling. Now, we will consider another type of non-linear gate that is generated by quadratic spin coupling. It is enough

if we have linear and quadratic spin interactions to generate arbitrary Dicke states because there will exist a control sequence which will get us from the initial state to our target state, although we may not know what the sequence is. However, if we have control with only operators that are linear in the collective spin, such as  $J^x$ ,  $J^z$ ,  $J^y$ , we can never go outside the algebra of the linear operators and thus do not have the ability to reach any arbitrary Dicke state. Even we have even one quadratic operator such as  $J^{z^2}$ , which is the choice of quadratic operator for our scheme, we will get out of our closed algebra of linear operators and access any Dicke state.

Our premise is an ensemble of spins in a cavity coupled linearly to a common bosonic mode. The cavity is described by the bosonic annihilation operator,  $a$  and creation operator,  $a^\dagger$  which follow the usual commutation relation  $[a, a^\dagger] = 1$ . The Hamiltonian,  $H$  of our system is given as

$$H = H_0 + \omega_0 J^z + 2g(a^\dagger + a)J^z = \omega a^\dagger a + \omega_0 J^z + 2g(a^\dagger + a)J^z, \quad (5.1)$$

where,  $H_0 = \omega a^\dagger a$  with  $\omega$  as mode frequency and  $g$  is the strength of linear coupling. The second term  $2g(a^\dagger + a)J^z$  in equation 5.1 represents the linear coupling of the spins to the bosonic mode. The Hamiltonian can be expressed in the interaction picture as  $H_I(t)$ .

$$H_I(t) = U^\dagger H U - H_0 = 2g(a^\dagger e^{i\omega t} + a e^{-i\omega t})J^z, \quad (5.2)$$

where,  $U = e^{iH_0 t}$ . The evolution  $U(t)$  can be found exactly by using Magnus expansion [84]. The solution is

$$\begin{aligned} U(t) &= \mathcal{T}(\exp(-i \int_0^t H_I(t') dt')) \\ &= e^{-i\beta(t)J^{z^2}} e^{-i(\alpha(t)a^\dagger + \alpha^*(t)a)J^z}, \end{aligned} \quad (5.3)$$

where  $\beta(t) = \left(\frac{2g}{\omega}\right)^2 (\sin(\omega t) - \omega t)$ ,  $\alpha(t) = \frac{(e^{i\omega t} - 1)2g}{i\omega}$  and  $\mathcal{T}$  is the time ordering operator. At time  $\tau = 2k\pi/\omega$  for  $k \in \mathbb{Z}$  we can cause the spins to decouple from the bosonic mode. Thus, the evolution operator for the spins,  $U(\tau)$  can be written as

$$U(\tau) = e^{i\delta J^{z^2}}, \quad (5.4)$$

where  $\delta = 8k\pi g^2/\omega^2$ . Therefore, following the above derivation, we will choose  $J^{z^2}$  as one of the control fields in an optimisation technique to prepare Dicke states in the Section 5.2.

An example of a physical system suitable for dynamics similar to our spin-cavity interactions can be found in the 2016 paper by Twamley et al [85] where the spins are Nitrogen Vacancy (NV) centres embedded in nanodiamonds coupled to a mechanical oscillator. The nanodiamond can be caused

to oscillate in the  $z$ -direction the system can be engineered so that a large magnetic field gradient along the  $z$ -axis facilitates linear coupling of spins to the oscillatory modes. The NV centres have three intrinsic spin states  $|-1\rangle$ ,  $|0\rangle$  and  $|1\rangle$ . Due to the application of specifically chosen magnetic field strength in the appropriate direction, only two of the three states,  $|-1\rangle$  and  $|0\rangle$  will contribute to the system dynamics and the third state,  $|1\rangle$  can be set off-resonant with a large detuning, effectively turning the NV centre into a two-level system.

## 5.2 Optimal control in QuTip

We do not have an analytic approach to prescribe the sequence of pulses we would require to go from our initial state to any target Dicke state. Nonetheless, we can take advantage of numerical packages to optimise for the pulse sequences. For our scheme, we chose QuTip which is a python package [86]. We will characterise our quantum system with 'drift' dynamics generator which represent dynamics that are invariant in time and 'control' dynamics generators which represent fields that can be manipulated externally. The QuTip package Qtrl helps us find the best possible state that is closest to our target state by setting up the drift, controls, system size, evolution parameters and some other important constraints as listed under 'input parameters' on table 5.1 that we might like to impose on our system. We choose a random initial control pulse and run the optimisation algorithm which outputs the plot of a new control pulse called the 'optimal control pulse'. This is the shape of the control pulse required to enable the state transformation of our choice. We obtain a final evolved state with a value of the fidelity error involved in the state preparation. We know that fidelity is a measure of how close the prepared state is to the ideal target quantum state. This means fidelity error is a measure of dissimilarity of the prepared and the target state. Fidelity error varies in value from 0 to 1, 0 implying a perfect state preparation where the prepared state exactly matches the target state and a value of 1 implying completely unsuccessful state preparation. The algorithm also gives other important details of state preparation such as the time required to reach the prepared state and the number of iterations among others. The main results of the optimisation algorithm for a system of  $N=20$  spins are listed under 'output parameters' in table 5.1. The algorithm can be modified to accommodate 'masking' in the control dynamics generators. A control mask is an array which helps us choose which control and at what time slots during the system evolution will stay unchanged while others evolve according to our Hamiltonian. Masks help carry out a smoother and faster optimisation. Details of this package can be found in the official QuTip documentation page [87].

Input data	
Parameter	Value
Number of spins	20
Number of time slots	50
Fidelity error target	0.001
Maximum number of iterations allowed	200
Maximum elapsed time allowed in seconds	120
Number of trials	15
Output data	
Parameter	Value
Lowest fidelity error without control amplitude bounds	0.000845
Lowest fidelity error with control amplitude bounds	0.003969
Number of iterations required	64
Time required for optimisation in seconds	0.545712

Table 5.1: Input and output data of the optimisation algorithm for N=20 spins.

### 5.3 Results

Here, we present the results of the optimisation algorithm for a system of N=20 spins. The initial state is the collective ground Dicke state,  $|J, -J\rangle$  and the target state is the state near the middle of the Dicke ladder,  $|J, 0\rangle$ . For the drift generator we choose  $J^z$  and for the controls we choose arbitrarily fast global rotations via  $J^x$ , where  $J^x$  alone is sufficient because we can generate any rotation with it, and the quadratic control  $J^{z2}$ . A mask is applied such that for a number of randomly chosen timeslots the evolution is inactive for the first control while active for the second control and vice versa for the rest of the timeslots. Active evolution means the control sequences evolve according to our chosen operator and inactive means it does not. Due to the random nature of the initial control pulse, we get different fidelities for different runs of the optimisation algorithm with the same input parameters. Thus, we run it multiple times to find the least fidelity error which gives us the best prepared state. This is also quoted in table 5.1 as the number of trials. The fidelity errors are calculated with and without upper and lower bounds on the control amplitudes of 1 and -1 respectively. We see that the fidelity error without bounds is about 4.7 times lower than that with bounds. However, for practical implementations,

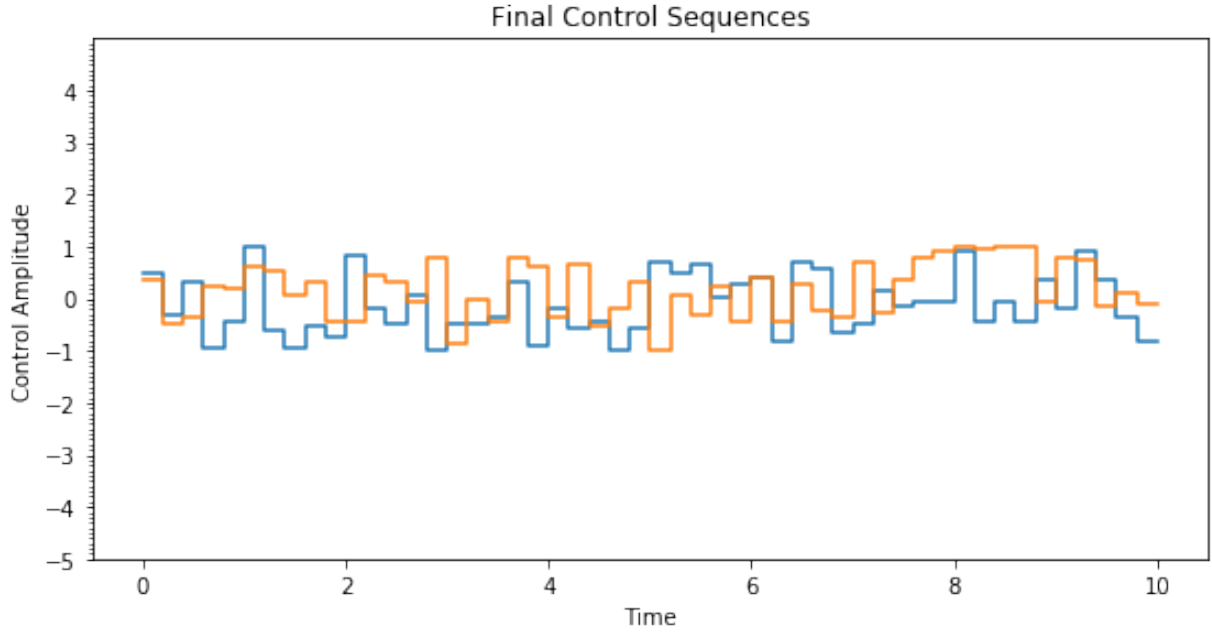


Figure 5.1: Plot of control pulses after optimisation for  $N=20$  spins.

control amplitude constraints are more realistic and therefore are important to account for. A plot of the control pulses corresponding to the two control fields,  $J^x$  and  $J^{z^2}$  for a system of  $N = 20$  spins after optimisation is shown in Figure 5.1. The final control sequence is important because it shows us the shape of the control sequence required for our  $|J, 0\rangle$  state preparation. We can change the number of spins,  $N$  as needed. However, the fidelity error rises with increasing  $N$  as shown in the plot of the fidelity error against  $N$  in Figure 5.2. Here, we have calculated fidelity errors for  $N$  ranging from 2 to 100. We can run the algorithm for greater  $N$  but there is a computational cost as the time of execution becomes rather long. We note that the fidelity error is low and increases at a slower rate up to approximately  $N = 22$ . There is a zoomed in portion of the plot as an inset that gives a clearer view of the slow rise of fidelity errors for  $N = 2$  to  $N = 22$ . As the number of spins increase beyond that, especially after  $N = 30$ , the fidelity error rises rapidly.

A number of factors might contribute to this rapid rise, one of which is due to keeping the number of timeslots fixed as  $N$  varied from 2 to 100. For greater number of spins, greater number of time slots could be applied which may decrease fidelity errors. We can infer this from Figure 5.3 which shows how increasing the number of timeslots from 25 to 50 gave lower fidelity errors with a flatter slope of rise when compared with fewer timeslots that caused fidelity errors to rise rapidly after about 10 spins. A second plot of how fidelity errors change when the number of trials is varied is shown in Figure 5.4 to determine whether increasing trial number may improve fidelities. We see that after

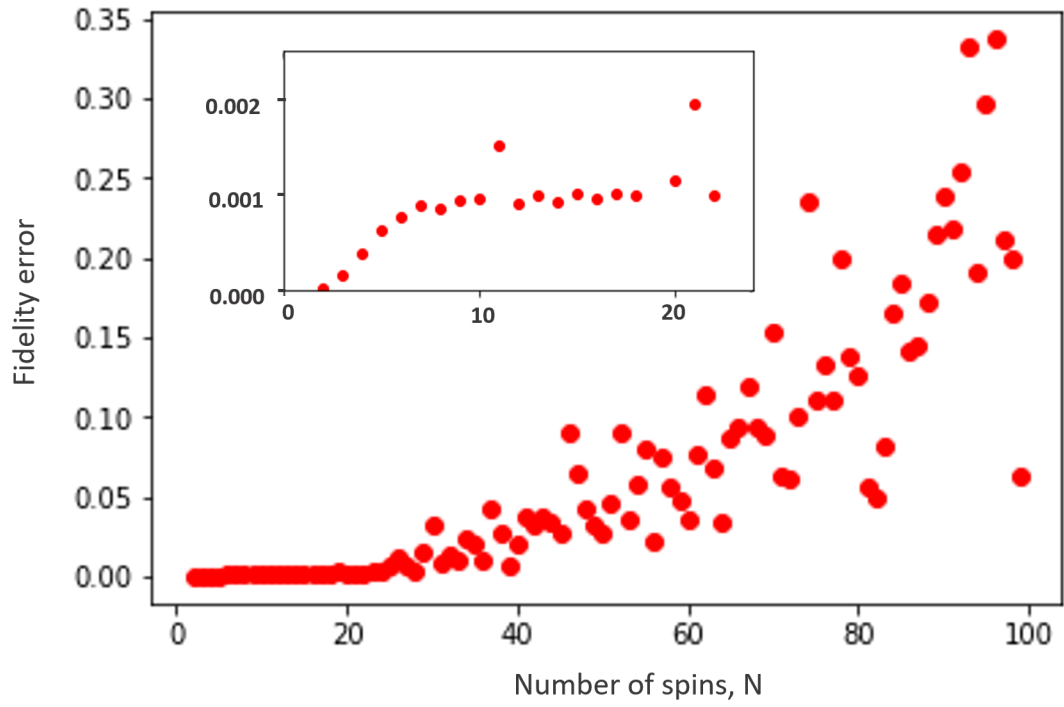


Figure 5.2: Fidelity errors for number of spins from  $N=2$  to 100, with a zoom inset from  $N=2$  to 22.

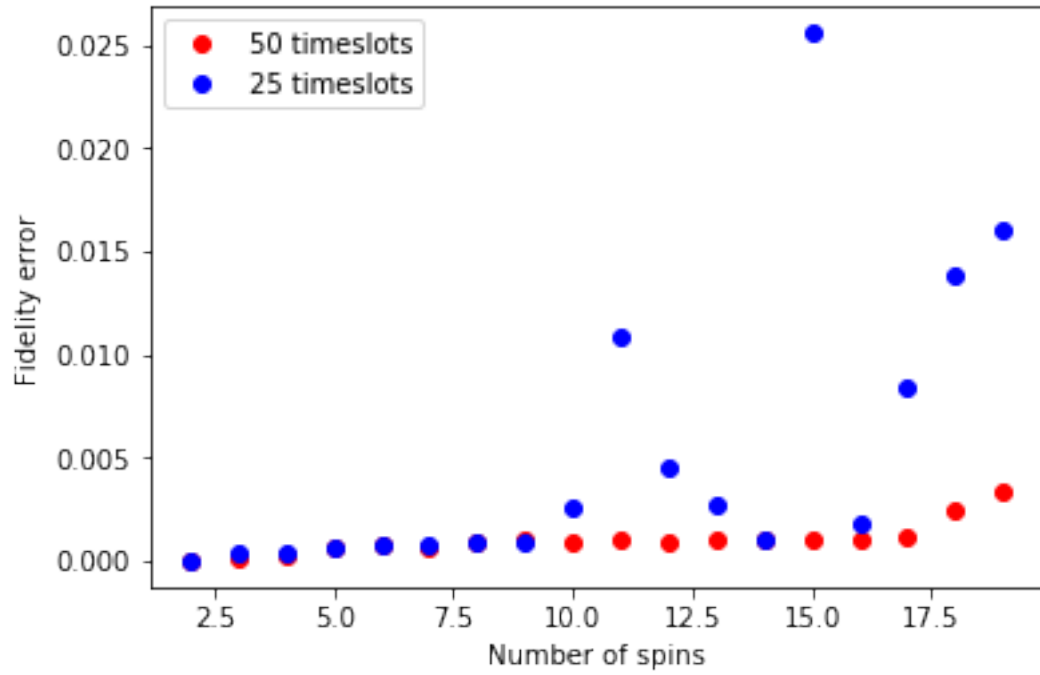


Figure 5.3: Fidelity error comparison for different number of timeslots.



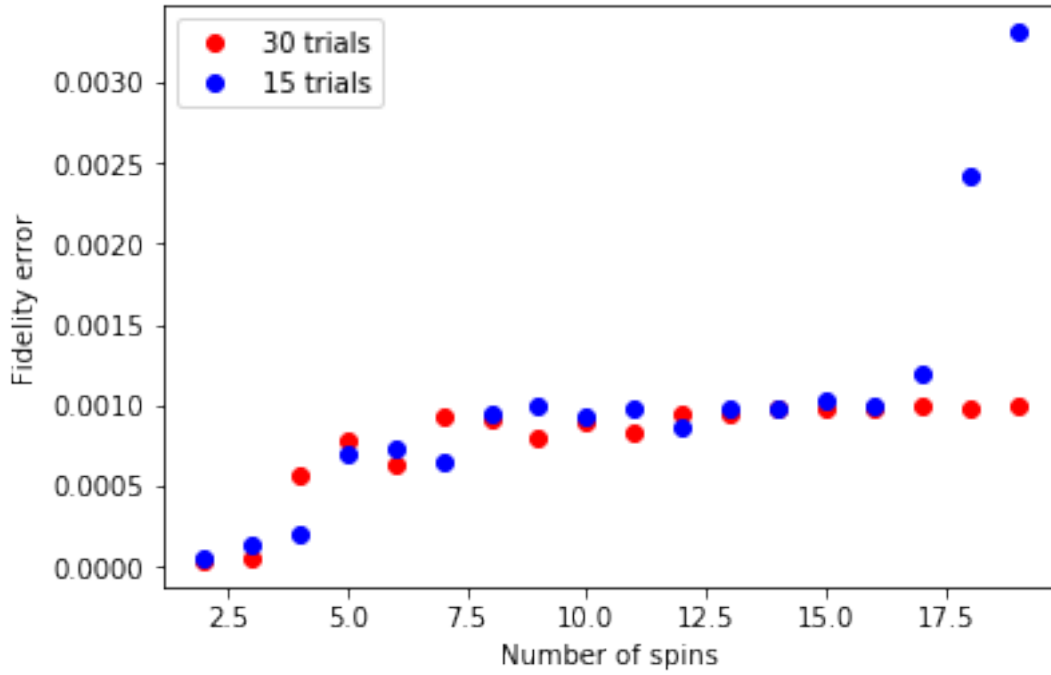


Figure 5.4: Fidelity error comparison for different number of trials.

about 16 spins, the fidelity error rise is much flatter for 30 trials compared to those for 15 trials. This may be another reason why the fidelity errors rise rapidly in Figure 5.2 as a fixed number of 15 trials was used for all values of  $N$ . How the timeslots and trials should scale with  $N$  has to be carefully determined by experimenting with different numbers for different ranges within  $N$ . The effect of other input parameters on fidelity could also be investigated and utilized to yield a better scaling of fidelities with number of spins. A quick comparison in fidelity values for  $N = 10$  spins of this optimal control method with our Grover method in 4 gives 99.9816% against 99.9069% which shows for smaller spin numbers, the optimal control method gives high fidelities but has relatively limited scalability in its current status. Thus, the optimal control method should be treated more thoroughly by varying different input parameters like number of trials, number of timeslots and initial control pulses to reach lower fidelity values and more stable fidelity scaling. Only then it would be possible to conduct a fair and proper comparison of this method with the Grover method in terms of efficiency of Dicke state preparation.



*"The most beautiful experience  
we can have is the mysterious. It  
is the fundamental emotion that  
stands at the cradle of true art  
and true science."*

- Albert Einstein

# 6

## Conclusion

In this thesis, we addressed the challenge of Dicke state preparation which is of great interest in quantum physics research. We explored three different methods to prepare Dicke states in an ensemble of spins. Although the methods discussed in the thesis can be used to prepare any Dicke state, almost all the calculations are based on preparing the half-excited collective state in the middle of the Dicke ladder because of its quantum enhanced absorption capabilities which can act as the essential state for building a superabsorbing system that could detect very weak light fields. The first method uses dipole-dipole interactions to break the Dicke degeneracy and enable selective transition along the Dicke ladder in steps using a sequence of  $\pi$ -pulses. The most important requirement here is the incorporation of the dipole-dipole interactions which we studied for linear and circular arrangement of dipoles, accounting for not just nearest neighbour interaction, but that among all the dipoles in the system. We found that the differential energy shift was greater for greater total interaction among the dipoles. We also analysed the scalability of this  $\pi$ -pulse method and found that power broadening effects, which are most prominent in the middle of the Dicke ladder, constrain the maximum feasible size of the spin ensemble. Thus, an alternative approach which gives high fidelities for large spin

ensembles was proposed as Method 2. It is a novel and exciting technique for preparing any arbitrary Dicke state using geometric phase gates in a Grover method. Unlike many other schemes, this method is much simpler with minimal control assumptions, independent of physical architecture of the system, requires no interaction between spins, selective addressing or special detunings. If we ignore the noise, this scheme shows an increase in fidelity with increasing number of spins. The preparation time for our desired state scales as  $O(N^{5/4})$ ,  $N$  being the number of spins, which is the best order for state preparations that involve a fully addressable quantum circuit. We also consider the dephasing processes that reduce our system coherence and described how the built-in dynamical decoupling can help combat the decoherence effects, thereby making the quantum protocol more efficient. We also studied how this method can prepare Dicke states capable of Heisenberg limited metrology and found that the superabsorptive Dicke state can attain the Heisenberg limited precision  $\Delta\nu = \frac{\sqrt{2}}{\sqrt{N(N+2)}}$ , where  $N$  is the number of spins in our case, with the  $J_z^2$  operator saturating the Cramér-Rao bound. This method can be implemented in a range of physical systems including the well-known NV centres in nanodiamonds, Rydberg atoms in a trap and superconducting qubits. The third and final method of state preparation involved spins linearly coupled to a common bosonic mode with induced quadratic spin interaction. Here, we optimised for the control pulse sequences required to reach any arbitrary Dicke state using optimal control algorithms in the numerical package QuTip. In this method, state preparation for smaller ensembles of spins gave high fidelities but the fidelity decreased as the number of spins were increased. Improvements to Method 3 could be made by varying input evolution parameters such as the number of trials and time slots for the optimisation algorithm but the appropriate scaling of these evolution parameters in terms of the number of spins need to be determined carefully. These will lead to an increase in fidelity of state preparation. Thus, within the scope of this thesis, the scalability of the optimal control method is concluded to be lower than the Grover method.

The suggested improvements to Method 3 could be carried out as an immediate extension of our project. For Method 2, an important future direction for further research would be to analyse how fidelities or phase sensitivity of state preparation scale with spin number in the presence of imperfections. There is interesting control theory that can be done given this useful set of resources of geometric phase gates, nonlinear gates and global controls. We have looked at only particular sequences for state preparation but it is possible to do more complicated sequences and determine the accessible set of states which can be obtained just using these unitary set of controls. Another important direction would be to address the challenge of quantum metrology using Dicke states more thoroughly by

including the effects of loss after we have prepared the state, that is, while waiting to accumulate the measurement signal. This is due to the fact that even though entangled states are powerful for accumulating information for a measurement signal, they are very fragile after preparation. Often times the signal to be measured is weak, so it might take time to measure it during which there could be decoherence. However, as explored in a very recent paper by Ouyang et al [88], one way to address this issue is to use superpositions of Dicke states as probes for metrology. These will be robust even in the presence of noise. Furthermore, we could consider a detailed experimental implementation of the Grover method where we take into account issues like inhomogeneities of the spins and their relevant decoherence channels. Other interesting aspects include considering a scheme where Dicke states that are prepared in the ground spin states are upconverted to optically excited states. For example, in case of the Nitrogen Vacancy (NV) centres, we can prepare Dicke states in the magnetic ground state, then do a transition to an optically excited state. This would be very sensitive to optical fields, as opposed to the states we looked into in this project that were sensitive to magnetic fields. Since we focused on the preparation of the superabsorptive Dicke state in this thesis, one outcome of this study is a possible future experimental project that could be carried out to test if NV centres embedded in nanodiamonds are feasible systems to demonstrate superabsorption as predicted through theory with the incorporation of more realistic parameters. A potential implementation is to combine the Grover technique with spins that will allow us to devise an efficient cycling of absorption at the transition of the superabsorptive Dicke state at the middle of the Dicke ladder to the state above it. This will require some form of reservoir engineering, such as that considered by Higgins et al [19] as mentioned in Chapter 1, so that the decay is restricted to a small subspace. Through further research into these exciting schemes and using this rich set of theoretical resources, we hope to develop a more robust understanding of quantum state preparations and quantum control strategies which will contribute to different areas of quantum metrology and quantum information.





## Appendix

### A.1 Alternative calculation to find total absorption rate for method 1.

This is the alternative calculation to find an exact form for the total absorption rate,  $\Gamma_i$  discussed in Chapter 3. The total absorption rate from the system of spins after using a  $\frac{\pi}{2}$ -pulse to excite the ground state  $|J, -J\rangle$  to state  $|\Psi_i\rangle$  can be expressed as:

$$\Gamma_i = \gamma \langle \Psi_i | J^- J^+ | \Psi_i \rangle = \gamma \langle J, -J | U^\dagger J^- J^+ U | J, -J \rangle, \quad (\text{A.1})$$

where  $\gamma$  is the free spin absorption rate,

$$U = e^{i\frac{\pi}{2}J^y},$$

$J^-$  and  $J^+$  are the total angular momentum lowering and raising operators for the collective spin states  $|J, M\rangle$ .

In equation A.1, we will focus on working out the expression  $U^\dagger J^- J^+ U$  and use it to calculate the

absorption rate.

$$\begin{aligned}
 & U^\dagger J^- J^+ U \\
 &= U^\dagger J^- (I) J^+ U, \text{ where } I \text{ is the identity matrix} \\
 &= U^\dagger J^- (U U^\dagger) J^+ U, \text{ as } I = U U^\dagger
 \end{aligned} \tag{A.2}$$

Now, consider  $U^\dagger J^+ U$  from the above expression.

$$\begin{aligned}
 & U^\dagger J^+ U \\
 &= U^\dagger (J^x + i J^y) U, \text{ as } J^+ = J^x + i J^y \\
 &= U^\dagger J^x U + U^\dagger i J^y U \\
 &= e^{-i\frac{\pi}{2} J^y} J^x e^{i\frac{\pi}{2} J^y} + e^{-i\frac{\pi}{2} J^y} i J^y e^{i\frac{\pi}{2} J^y}
 \end{aligned} \tag{A.3}$$

Note:

$$\begin{aligned}
 U^\dagger i J^y U &= e^{-i\frac{\pi}{2} J^y} i J^y e^{i\frac{\pi}{2} J^y} \\
 &= i J^y + i \frac{\pi}{2} [J^y, J^y] = i J^y, \text{ as } [J^y, J^y] = 0
 \end{aligned} \tag{A.4}$$

So, that leaves us with working out an expression for  $U^\dagger J^x U = e^{-i\frac{\pi}{2} J^y} J^x e^{i\frac{\pi}{2} J^y}$ .

Let  $f(\theta) = U^\dagger J^x U = e^{-i\theta J^y} J^x e^{i\theta J^y}$ . Then, the first and second derivatives,  $f'(\theta)$  and  $f''(\theta)$  respectively are calculated as:

$$\begin{aligned}
 f'(\theta) &= \frac{d}{d\theta} (e^{-i\theta J^y} J^x e^{i\theta J^y}) \\
 &= e^{-i\theta J^y} (-i J^y J^x) e^{i\theta J^y} + e^{-i\theta J^y} (J^x i J^y) e^{i\theta J^y} \\
 &= e^{-i\theta J^y} \cdot -i [J^y, J^x] \cdot e^{i\theta J^y} \\
 &= e^{-i\theta J^y} \cdot -J^z \cdot e^{i\theta J^y}, \text{ as } [J^y, J^x] = -i J^z
 \end{aligned}$$

$$\begin{aligned}
 f''(\theta) &= \frac{d}{d\theta} (e^{-i\theta J^y} \cdot -J^z \cdot e^{i\theta J^y}) \\
 &= -(e^{-i\theta J^y} (-i J^y J^z) e^{-i\theta J^y} + e^{-i\theta J^y} (i J^z J^y) e^{-i\theta J^y}) \\
 &= e^{-i\theta J^y} \cdot -i [J^y J^z] \cdot e^{-i\theta J^y} \\
 &= -e^{-i\theta J^y} J^x e^{-i\theta J^y}, \text{ as } [J^y, J^z] = i J^x
 \end{aligned}$$

We note that:



$$f''(\theta) = -f(\theta) \text{ [2nd order ODE that we will solve to find } f(\theta)] \quad (\text{A.5})$$

Initial conditions:

$$f(\theta = 0) = J^x \quad (\text{A.6})$$

$$f'(\theta = 0) = -J^z \quad (\text{A.7})$$

Trial solution:

$$\text{Let } f(\theta) = Ae^{i\theta} + Be^{-i\theta} \quad (\text{A.8})$$

$$\text{Then, } f'(\theta) = iAe^{i\theta} - iBe^{-i\theta} \quad (\text{A.9})$$

We can find constants  $A, B$  by imposing initial conditions A.7 on the trial expressions for  $f(\theta)$  and  $f'(\theta)$ .

That is,

$$f(0) = A + B = J^x \quad (\text{A.10})$$

$$f'(0) = i(A - B) = -J^z \quad (\text{A.11})$$

$$\implies A = \frac{J^x + iJ^z}{2}, B = \frac{J^x - iJ^z}{2}$$

So, putting the expressions for  $A$  and  $B$  in equation A.8 we get:

$$\begin{aligned} f(\theta) &= \frac{J^x + iJ^z}{2}e^{i\theta} + \frac{J^x - iJ^z}{2}e^{-i\theta} \\ &= J^x \frac{e^{i\theta} + e^{-i\theta}}{2} + J^z i^2 \frac{e^{i\theta} - e^{-i\theta}}{2i} \\ &= J^x \cos(\theta) - J^z \sin(\theta), \text{ as } \frac{e^{i\theta} + e^{-i\theta}}{2} = \cos(\theta) \text{ and } \frac{e^{i\theta} - e^{-i\theta}}{2i} = \sin(\theta) \end{aligned} \quad (\text{A.12})$$

For  $\theta = \frac{\pi}{2}$ :

$$f(\theta) = U^\dagger J^x U = J^x \cos\left(\frac{\pi}{2}\right) - J^z \sin\left(\frac{\pi}{2}\right) = -J^z \quad (\text{A.13})$$

So, our expression  $U^\dagger J^- J^+ U$  from A.2 can be now written as:

$$\begin{aligned} U^\dagger J^- J^+ U &= (U^\dagger J^- U)(U^\dagger J^+ U) \\ &= (-J^z - iJ^y)(-J^z + iJ^y) \\ &= (J^z)^2 - iJ^z J^y + iJ^y J^z + (J^y)^2 \\ &= (J^z)^2 + i[J^y, J^z] + (J^y)^2 \\ &= (J^z)^2 - J^x + (J^y)^2 \end{aligned} \quad (\text{A.14})$$

The absorption rate,  $\Gamma_i$  from equation A.1 is then given by:

$$\begin{aligned}\Gamma_i &= \gamma \langle J, -J | (J^z)^2 - J^x + (J^y)^2 | J, -J \rangle \\ &= \gamma \left( (-J)^2 + 0 + \langle J, -J | (J^y)^2 | J, -J \rangle \right)\end{aligned}\quad (\text{A.15})$$

Here,

$$\begin{aligned}\langle J, -J | (J^y)^2 | J, -J \rangle &= \langle J, -J | \left( \frac{J^+ - J^-}{2i} \right)^2 | J, -J \rangle \\ &= \langle J, -J | \left( -\frac{1}{4} ((J^+)^2 - J^+ J^- - J^- J^+ + (J^-)^2) \right) | J, -J \rangle \\ &= 0 + 0 + \left( -\frac{1}{4} - 2J \right) + 0 \\ &= \frac{J}{2}\end{aligned}\quad (\text{A.16})$$

Thus,  $\Gamma_i = \gamma(J^2 + \frac{J}{2})$ .

# References

- [1] M. T. Johnsson, N. R. Mukty, D. Burgarth, T. Volz, and G. K. Brennen. *Scalable preparation of dicke states for quantum sensing*. arXiv preprint arXiv:1908.01120 (2019).
- [2] J. K. Stockton, J. Geremia, A. C. Doherty, and H. Mabuchi. *Characterizing the entanglement of symmetric many-particle spin-1/2 systems*. Physical Review A **67**(2), 022112 (2003).
- [3] M. Koashi, V. Bužek, and N. Imoto. *Entangled webs: Tight bound for symmetric sharing of entanglement*. Physical Review A **62**(5), 050302 (2000).
- [4] A. Cabello. *Bell's theorem with and without inequalities for the three-qubit greenberger-horne-zeilinger and w states*. Physical Review A **65**(3), 032108 (2002).
- [5] G. Tóth. *Multipartite entanglement and high-precision metrology*. Physical Review A **85**(2), 022322 (2012).
- [6] R. Prevedel, G. Cronenberg, M. S. Tame, M. Paternostro, P. Walther, M.-S. Kim, and A. Zeilinger. *Experimental realization of dicke states of up to six qubits for multiparty quantum networking*. Physical review letters **103**(2), 020503 (2009).
- [7] A. I. Lvovsky, B. C. Sanders, and W. Tittel. *Optical quantum memory*. Nature photonics **3**(12), 706 (2009).
- [8] S. K. Özdemir, J. Shimamura, and N. Imoto. *A necessary and sufficient condition to play games in quantum mechanical settings*. New Journal of Physics **9**(2), 43 (2007).
- [9] C. Zhu, F. Xu, and C. Pei. *W-state analyzer and multi-party measurement-device-independent quantum key distribution*. Scientific reports **5**, 17449 (2015).

- 
- [10] J. K. Stockton, R. van Handel, and H. Mabuchi. *Deterministic dicke-state preparation with continuous measurement and control*. Physical Review A **70**(2), 022106 (2004).
- [11] Y.-F. Xiao, X.-B. Zou, and G.-C. Guo. *Generation of atomic entangled states with selective resonant interaction in cavity quantum electrodynamics*. Physical Review A **75**(1), 012310 (2007).
- [12] X.-Q. Shao, L. Chen, S. Zhang, Y.-F. Zhao, and K.-H. Yeon. *Deterministic generation of arbitrary multi-atom symmetric dicke states by a combination of quantum zeno dynamics and adiabatic passage*. EPL (Europhysics Letters) **90**(5), 50003 (2010).
- [13] D. Hume, C.-W. Chou, T. Rosenband, and D. J. Wineland. *Preparation of dicke states in an ion chain*. Physical Review A **80**(5), 052302 (2009).
- [14] L. Lamata, C. E. Lopez, B. Lanyon, T. Bastin, J. C. Retamal, and E. Solano. *Deterministic generation of arbitrary symmetric states and entanglement classes*. Physical Review A **87**(3), 032325 (2013).
- [15] S. S. Ivanov, N. V. Vitanov, and N. V. Korolkova. *Creation of arbitrary dicke and noon states of trapped-ion qubits by global addressing with composite pulses*. New Journal of Physics **15**(2), 023039 (2013).
- [16] W. Wieczorek, R. Krischek, N. Kiesel, P. Michelberger, G. Tóth, and H. Weinfurter. *Experimental entanglement of a six-photon symmetric dicke state*. Physical review letters **103**(2), 020504 (2009).
- [17] C. Wu, C. Guo, Y. Wang, G. Wang, X.-L. Feng, and J.-L. Chen. *Generation of dicke states in the ultrastrong-coupling regime of circuit qed systems*. Physical Review A **95**(1), 013845 (2017).
- [18] A. Bäertschi and S. Eidenbenz. *Deterministic preparation of dicke states*. arXiv preprint arXiv:1904.07358 (2019).
- [19] K. Higgins, S. Benjamin, T. Stace, G. Milburn, B. W. Lovett, and E. Gauger. *Superabsorption of light via quantum engineering*. Nature communications **5**, 4705 (2014).
- [20] L. Maccone and V. Giovannetti. *Quantum metrology: Beauty and the noisy beast*. Nature Physics **7**(5), 376 (2011).

- [21] K. Banaszek, R. Demkowicz-Dobrzański, and I. A. Walmsley. *Quantum states made to measure*. Nature Photonics **3**(12), 673 (2009).
- [22] M. G. Paris. *Quantum estimation for quantum technology*. International Journal of Quantum Information **7**(supp01), 125 (2009).
- [23] V. Giovannetti, S. Lloyd, and L. Maccone. *Advances in quantum metrology*. Nature photonics **5**(4), 222 (2011).
- [24] R. Demkowicz-Dobrzański, J. Kołodyński, and M. Guță. *The elusive heisenberg limit in quantum-enhanced metrology*. Nature communications **3**, 1063 (2012).
- [25] Y. Matsuzaki and S. Benjamin. *Magnetic-field sensing with quantum error detection under the effect of energy relaxation*. Physical Review A **95**(3), 032303 (2017).
- [26] W. Dür, M. Skotiniotis, F. Froewis, and B. Kraus. *Improved quantum metrology using quantum error correction*. Physical Review Letters **112**(8), 080801 (2014).
- [27] D. Gottesman. *An introduction to quantum error correction and fault-tolerant quantum computation*. In *Quantum information science and its contributions to mathematics, Proceedings of Symposia in Applied Mathematics*, vol. 68, pp. 13–58 (2010).
- [28] G. Arrad, Y. Vinkler, D. Aharonov, and A. Retzker. *Increasing sensing resolution with error correction*. Physical review letters **112**(15), 150801 (2014).
- [29] X.-M. Lu, S. Yu, and C. Oh. *Robust quantum metrological schemes based on protection of quantum fisher information*. Nature communications **6**, 7282 (2015).
- [30] S. Zhou, M. Zhang, J. Preskill, and L. Jiang. *Achieving the heisenberg limit in quantum metrology using quantum error correction*. Nature communications **9**(1), 78 (2018).
- [31] S. D. Bartlett, G. K. Brennen, and A. Miyake. *Robust symmetry-protected metrology with the haldane phase*. Quantum Science and Technology **3**(1), 014010 (2017).
- [32] R. H. Dicke. *Coherence in spontaneous radiation processes*. Physical review **93**(1), 99 (1954).
- [33] M. Gross and S. Haroche. *Superradiance: An essay on the theory of collective spontaneous emission*. Physics reports **93**(5), 301 (1982).

- [34] J. C. MacGillivray and M. Feld. *Theory of superradiance in an extended, optically thick medium*. Physical Review A **14**(3), 1169 (1976).
- [35] R. Bonifacio, P. Schwendimann, and F. Haake. *Quantum statistical theory of superradiance. ii*. Physical Review A **4**(3), 854 (1971).
- [36] M. Moore and P. Meystre. *Theory of superradiant scattering of laser light from bose-einstein condensates*. Physical Review Letters **83**(25), 5202 (1999).
- [37] K. Cong, Q. Zhang, Y. Wang, G. T. Noe, A. Belyanin, and J. Kono. *Dicke superradiance in solids*. JOSA B **33**(7), C80 (2016).
- [38] M. G. Benedict. *Super-radiance: Multiatomic coherent emission* (Routledge, 2018).
- [39] N. Skribanowitz, I. Herman, J. MacGillivray, and M. Feld. *Observation of dicke superradiance in optically pumped hf gas*. Physical Review Letters **30**(8), 309 (1973).
- [40] F. Gounand, M. Hugon, P. Fournier, and J. Berlande. *Superradiant cascading effects in rubidium rydberg levels*. Journal of Physics B: Atomic and Molecular Physics **12**(4), 547 (1979).
- [41] Y. Kaluzny, P. Goy, M. Gross, J. Raimond, and S. Haroche. *Observation of self-induced rabi oscillations in two-level atoms excited inside a resonant cavity: The ringing regime of superradiance*. Physical review letters **51**(13), 1175 (1983).
- [42] R. DeVoe and R. Brewer. *Observation of superradiant and subradiant spontaneous emission of two trapped ions*. Physical review letters **76**(12), 2049 (1996).
- [43] J. A. Mlynek, A. A. Abdumalikov, C. Eichler, and A. Wallraff. *Observation of dicke superradiance for two artificial atoms in a cavity with high decay rate*. Nature communications **5**, 5186 (2014).
- [44] C. Bradac, M. T. Johnsson, M. van Breugel, B. Q. Baragiola, R. Martin, M. L. Juan, G. K. Brennen, and T. Volz. *Room-temperature spontaneous superradiance from single diamond nanocrystals*. Nature communications **8**(1), 1205 (2017).
- [45] M. Gross, C. Fabre, P. Pillet, and S. Haroche. *Observation of near-infrared dicke superradiance on cascading transitions in atomic sodium*. Physical Review Letters **36**(17), 1035 (1976).
- [46] P. Goy, L. Moi, M. Gross, J. Raimond, C. Fabre, and S. Haroche. *Rydberg-atom masers. ii. triggering by external radiation and application to millimeter-wave detectors*. Physical Review A **27**(4), 2065 (1983).

- [47] R. Florian, L. Schwan, and D. Schmid. *Superradiance and high-gain mirrorless laser activity of o- 2-centers in kcl*. Solid State Communications **42**(1), 55 (1982).
- [48] O. Varnavskii, A. Kirkin, A. Leontovich, R. Malikov, A. Mozharovskii, and E. Trifonov. *Coherent amplification of ultrashort pulses in activated crystals*. Zhurnal Eksperimental'noi i Teoreticheskoi Fiziki **86**, 1227 (1984).
- [49] P. Varnavskii, V. Golovlev, A. Kirkin, R. Malikov, and A. Mozharovskii. *Coherent propagation of small-area pulses in activated crystals*. Zh. Eksp. Teor. Fiz **90**, 1596 (1986).
- [50] M. Scheibner, T. Schmidt, L. Worschech, A. Forchel, G. Bacher, T. Passow, and D. Hommel. *Superradiance of quantum dots*. Nature Physics **3**(2), 106 (2007).
- [51] A. Angerer, K. Streltsov, T. Astner, S. Putz, H. Sumiya, S. Onoda, J. Isoya, W. J. Munro, K. Nemoto, J. Schmiedmayer, *et al.* *Superradiant emission from colour centres in diamond*. Nature Physics **14**(12), 1168 (2018).
- [52] R. Monshouwer, M. Abrahamsson, F. Van Mourik, and R. Van Grondelle. *Superradiance and exciton delocalization in bacterial photosynthetic light-harvesting systems*. The Journal of Physical Chemistry B **101**(37), 7241 (1997).
- [53] J. G. Bohnet, Z. Chen, J. M. Weiner, D. Meiser, M. J. Holland, and J. K. Thompson. *A steady-state superradiant laser with less than one intracavity photon*. Nature **484**(7392), 78 (2012).
- [54] A. T. Black, J. K. Thompson, and V. Vuletić. *On-demand superradiant conversion of atomic spin gratings into single photons with high efficiency*. Physical review letters **95**(13), 133601 (2005).
- [55] A. Kuzmich, W. Bowen, A. Boozer, A. Boca, C. Chou, L.-M. Duan, and H. Kimble. *Generation of nonclassical photon pairs for scalable quantum communication with atomic ensembles*. Nature **423**(6941), 731 (2003).
- [56] C. H. van der Wal, M. D. Eisaman, A. André, R. L. Walsworth, D. F. Phillips, A. S. Zibrov, and M. D. Lukin. *Atomic memory for correlated photon states*. Science **301**(5630), 196 (2003).
- [57] M. H. Van Putten. *Superradiance in a torus magnetosphere around a black hole*. Science **284**(5411), 115 (1999).
- [58] D. F. Walls and G. J. Milburn. *Quantum optics* (Springer Science & Business Media, 2007).

- [59] A. P. Alivisatos. *Semiconductor clusters, nanocrystals, and quantum dots*. science **271**(5251), 933 (1996).
- [60] N. Manson, J. Harrison, and M. Sellars. *Nitrogen-vacancy center in diamond: Model of the electronic structure and associated dynamics*. Physical Review B **74**(10), 104303 (2006).
- [61] C. Hepp, T. Müller, V. Waselowski, J. N. Becker, B. Pingault, H. Sternschulte, D. Steinmüller-Nethl, A. Gali, J. R. Maze, M. Atatüre, *et al.* *Electronic structure of the silicon vacancy color center in diamond*. Physical Review Letters **112**(3), 036405 (2014).
- [62] M. G. Dutt, L. Childress, L. Jiang, E. Togan, J. Maze, F. Jelezko, A. Zibrov, P. Hemmer, and M. Lukin. *Quantum register based on individual electronic and nuclear spin qubits in diamond*. Science **316**(5829), 1312 (2007).
- [63] G. Agarwal. *Quantum optics, vol. 70 of springer tracts in modern physics* (1974).
- [64] B. Coffey and R. Friedberg. *Effect of short-range coulomb interaction on cooperative spontaneous emission*. Physical Review A **17**(3), 1033 (1978).
- [65] B. Richards and R. Jones. *Dipole-dipole resonance line shapes in a cold rydberg gas*. Physical Review A **93**(4), 042505 (2016).
- [66] J. J. Sakurai, J. Napolitano, *et al.* *Modern quantum mechanics*, vol. 185 (Pearson Harlow, 2014).
- [67] M. A. Nielsen and I. Chuang. *Quantum computation and quantum information* (2002).
- [68] W. Demtröder. *Laser spectroscopy: vol. 1: basic principles*, vol. 1 (Springer Science & Business Media, 2008).
- [69] P. Neumann, R. Kolesov, B. Naydenov, J. Beck, F. Rempp, M. Steiner, V. Jacques, G. Balasubramanian, M. Markham, D. Twitchen, *et al.* *Quantum register based on coupled electron spins in a room-temperature solid*. Nature Physics **6**(4), 249 (2010).
- [70] D. James and J. Jerke. *Effective hamiltonian theory and its applications in quantum information*. Canadian Journal of Physics **85**(6), 625 (2007).
- [71] L. Jiang, G. K. Brennen, A. V. Gorshkov, K. Hammerer, M. Hafezi, E. Demler, M. D. Lukin, and P. Zoller. *Anyonic interferometry and protected memories in atomic spin lattices*. Nature Physics **4**(6), 482 (2008).



- [72] G. K. Brennen, K. Hammerer, L. Jiang, M. D. Lukin, and P. Zoller. *Global operations for protected quantum memories in atomic spin lattices*. arXiv preprint arXiv:0901.3920 (2009).
- [73] E. L. Hahn. *Spin echoes*. Physical review **80**(4), 580 (1950).
- [74] H. Y. Carr and E. M. Purcell. *Effects of diffusion on free precession in nuclear magnetic resonance experiments*. Physical review **94**(3), 630 (1954).
- [75] G. Agarwal. *Saving entanglement via a nonuniform sequence of  $\pi$  pulses*. Physica Scripta **82**(3), 038103 (2010).
- [76] H. Cramér. *Mathematical methods of statistics*, vol. 9 (Princeton university press, 1999).
- [77] I. Apellaniz, B. Lücke, J. Peise, C. Klempt, and G. Tóth. *Detecting metrologically useful entanglement in the vicinity of dicke states*. New Journal of Physics **17**(8), 083027 (2015).
- [78] C. Sayrin, I. Dotsenko, X. Zhou, B. Peaudecerf, T. Rybarczyk, S. Gleyzes, P. Rouchon, M. Mirrahimi, H. Amini, M. Brune, *et al.* *Real-time quantum feedback prepares and stabilizes photon number states*. Nature **477**(7362), 73 (2011).
- [79] M. Stammeier, S. García, T. Thiele, J. Deiglmayr, J. A. Agner, H. Schmutz, F. Merkt, and A. Wallraff. *Measuring the dispersive frequency shift of a rectangular microwave cavity induced by an ensemble of rydberg atoms*. Physical Review A **95**(5), 053855 (2017).
- [80] C. Wang, Y. Y. Gao, P. Reinhold, R. W. Heeres, N. Ofek, K. Chou, C. Axline, M. Reagor, J. Blumoff, K. Sliwa, *et al.* *A schrödinger cat living in two boxes*. Science **352**(6289), 1087 (2016).
- [81] M. Lee, K. Friebe, D. A. Fioretto, K. Schüppert, F. R. Ong, D. Plankensteiner, V. Torggler, H. Ritsch, R. Blatt, and T. E. Northup. *Ion-based quantum sensor for optical cavity photon numbers*. Physical review letters **122**(15), 153603 (2019).
- [82] J. Pedernales, I. Lizuain, S. Felicetti, G. Romero, L. Lamata, and E. Solano. *Quantum rabi model with trapped ions*. Scientific reports **5**, 15472 (2015).
- [83] T. Astner, S. Nevlacsil, N. Peterschofsky, A. Angerer, S. Rotter, S. Putz, J. Schmiedmayer, and J. Majer. *Coherent coupling of remote spin ensembles via a cavity bus*. Physical review letters **118**(14), 140502 (2017).

- 
- [84] S. Blanes, F. Casas, J. Oteo, and J. Ros. *A pedagogical approach to the magnus expansion*. European Journal of Physics **31**(4), 907 (2010).
- [85] K. Xia, J. Twamley, *et al.* *Generating spin squeezing states and greenberger-horne-zeilinger entanglement using a hybrid phonon-spin ensemble in diamond*. Physical Review B **94**(20), 205118 (2016).
- [86] P. N. et al. *Qutip* (2013). URL <http://qutip.org/>.
- [87] P. N. et al. *Quantum optimal control* (2011). URL <http://qutip.org/docs/latest/guide/guide-control.html>.
- [88] Y. Ouyang, N. Shettell, and D. Markham. *Robust quantum metrology with explicit symmetric states*. arXiv preprint arXiv:1908.02378 (2019).